Wind Turbine and Slip Permanent Magnet Coupler Design Analysis for Small Scale Fixed Speed Wind Generator Systems

by

Niniva Dumakude

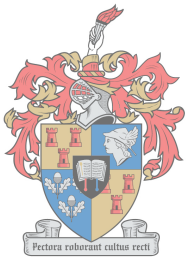

UNIVERSITEIT
iYUNIVESITHI
STELLENBOSCH
UNIVERSITY

Thesis presented in partial fulfilment of the requirements for the degree of Master of Science in Electrical and Electronic Engineering in the Faculty of Engineering at Stellenbosch University

Supervisor: Prof. M.J. Kamper

March 2018

Stellenbosch University https://scholar.sun.ac.za

Declaration

By submitting this thesis electronically, I declare that the entirety of the work contained therein is my own, original work, that I am the sole author thereof (save to the extent explicitly otherwise stated), that reproduction and publication thereof by Stellenbosch University will not infringe any third party rights and that I have not previously in its entirety or in part submitted it for obtaining any qualification.

Date: .....

Copyright © 2018 Stellenbosch University
All rights reserved.

Stellenbosch University https://scholar.sun.ac.za

Abstract

Wind Turbine and Slip Permanent Magnet Coupler Design Analysis for Small Scale Fixed Speed Wind Generator Systems

N. Dumakude

Department of Electrical and Electronic Engineering,
University of Stellenbosch,
Private Bag X1, Matieland 7602, South Africa.

Thesis: MScEng (Elec)

March 2018

Very recently has the concept of a slip coupler been introduced in wind energy applications. It forms part of the SS-PMG and there is extensive work being done in evaluating the technology. It's application is for a fixed speed and fixed blade pitch stall controlled wind turbine. The stall controlled wind turbine's aerodynamic performance is evaluated using BEM and CFD for various wind conditions where the gust winds are evaluated in case they pose a potential threat in the health of the system components. The optimum energy capture for proposed wind site is established and a cost analysis is performed in order to establish what size turbine and cost would yield optimum energy production per cost. A cost model for the SS-PMG system is proposed whereby a discrete cost package for the slip-PMC and the PMSG are developed, with the use of mass ratios of the SS-PMG components and some data from electrical machines manufacturers. A simple cost model for the wind turbine blades is established and with the available cost models, the drive train cost evaluation is performed in evaluating the competitiveness of the Aero Energy and the NREL Phase VI wind turbine. To minimise shaft stiffness, the slip-PMC is introduced in small-scale wind turbines. The analysis of such machines is proposed and evaluated. A spoke-mount PM coupler configuration is proposed and its performance is evaluated against that of the the surface-mount PM coupler which is widely studied in most literature. The machine performance sensitivity to magnet dimensions is done in a form of a optimisation of a PM rotor for a fixed wound rotor. The spoke-mount PM machine shows an improvement in torque performance for the same amount of PM material as the

Stellenbosch University https://scholar.sun.ac.za

surface-mount PM machine. The slip-PMC torque performance is dependent on the effective resistance of the coils, thus assuming dc resistance only yields inaccurate prediction, especially at high frequencies. Thus slot leakage effect is accounted by introducing a multiple layer coil modelling technique whereby the average taken when only one coil layer is considered is minimised. Additionally the ac resistance is dominant where the skin depth of penetration is less than the actual coil depth, thus it is deemed necessary to evaluate the model performance assuming ac resistance at high slip frequencies. The low core loss which is deemed negligible in the design optimisation of such a machine is demonstrated using a static and time harmonic model. The conduction losses which are quite dominant and accounted for in the design optimisation are illustrated. Finally the slip-PMC concept is tested test rig prototype which shows is in agreement with the static FEM analysis method, in effect validating the slip-PMC concept.

Stellenbosch University https://scholar.sun.ac.za

Uittreksel

Windturbine en Slip Permanent Magnet Coupler Ontwerp Analise vir Kleinskaal Vaste Spoed Wind Generator Systems

("Wind Turbine and Slip PM Coupler Design Analysis for Small Scale Fixed Speed Wind Generator Systems")

N. Dumakude

Departement Elektriese en Elektronies Ingenieurswese,
Universiteit van Stellenbosch,
Privaatsak X1, Matieland 7602, Suid Afrika.

Tesis: MScIng (Elek)

Maart 2018

Baie onlangs is die konsep van 'n glipkoppelaar in windenergie-toepassings bekendgestel. Dit vorm deel van die SS-PMG en daar word uitgebreide werk gedoen om die tegnologie te evalueer. Dit is die toepassing van 'n vaste spoed-en-vaste-mes-stalletjie beheerde windturbine. Die aërodinamiese prestasie van die stalletriese windturbine word geëvalueer met behulp van BEM en CFD vir verskeie windtoestande waar die windwinde geëvalueer word in die geval dat dit 'n potensiële bedreiging in die gesondheid van die stelselkomponente inhou. Die optimale energie-opname vir die voorgestelde windterrein word vasgestel en 'n koste-analise word uitgevoer om vas te stel watter grootte turbine en koste optimale energieproduksie per koste sal lewer. 'N Kostemodel vir die SS-PMG-stelsel word voorgestel waarvolgens 'n diskrete kostepakket vir die slip-PMC en die PMSG ontwikkel word, met behulp van massaverhoudings van die SS-PMG komponente en sommige data van vervaardigers van elektriese masjiene. 'N Eenvoudige kostemodel vir die windturbine-lemme word gevestig. Met die beskikbare kostemodelle word die koste-evaluering van die treinkoste uitgevoer om die mededingendheid van die Aero Energy en die wind turbine van die NREL Fase VI te evalueer. Om die styfheid van die skag te verminder, word die slip-PMC in kleinschalige windturbines ingevoer. Die ontleding van sulke masjiene word voorgestel en geëvalueer. 'N Spreek-berg-PM-koppelaarkonfigurasie word voorgestel en sy prestasie word geëvalueer teen dié van die oppervlakmonteer-PM-koppelaar wat in die meeste literatuur wyd

Stellenbosch University https://scholar.sun.ac.za

bestudeer word. Die masjienprestasie sensitiwiteit vir magneet afmetings word gedoen in 'n vorm van 'n optimalisering van 'n PM rotor vir 'n vaste wondrotor. Die geperforeerde PM-masjien toon 'n verbetering in wringkragprestasie vir dieselfde hoeveelheid PM-materiaal as die oppervlakmonterende PM-masjien. Die glip-PMC-wringkragprestasie is afhanklik van die effektiewe weerstand van die spoele, dus aanvaar die dc weerstand slegs onakkurate voorspelling, veral by hoë frekwensies. So die slot lek effek word verantwoord deur die invoering van 'n meervoudige laag spoel modellering tegniek waardeur die gemiddelde geneem wanneer slegs een spoel laag oorweeg word, word geminimaliseer. Daarbenewens is die AC-weerstand dominante waar die veldigtheid van die penetrasie minder is as die werklike spoeldiepte. Dit word dus nodig geag om die modelprestasie te evalueer met die aanvaarding van AC-weerstand teen hoë glyfrekwensies. Die lae kernverlies wat onbeduidend geag word in die ontwerpoptimalisering van so 'n masjien word gedemonstreer met behulp van 'n statiese en tyd harmoniese model. Die geleidelike verliese wat heeltemal oorheersend en verantwoord word in die ontwerpoptimalisering word geïllustreer. Ten slotte word die slip-PMC-konsep getoets met die toets-prototipe wat toon dat dit in ooreenstemming is met die statiese FEM-analise-metode, wat die slip-PMC-konsep uiteindelik bevestig.

Stellenbosch University https://scholar.sun.ac.za

Acknowledgements

I would like to express my sincere gratitude to the following people and organisations:

- Prof. Maarten J. Kamper for his support and guidance during this journey.
- The National Research Foundation (NRF) of South Africa for the generous financial assistance.
- Charl Moller for assisting me with the crash course on how to optimally utilize the High Performance Computing (HPC) facility of Stellenbosch University.
- Stiaan Gerber for assisting with the Stellenbosch Electric Machine Finite Element Method (SEMFEM) code implementations that accommodated the research objectives.
- The Electric Machines Laboratory (EMLAB) staff for their technical support.
- My family for their unwavering love and support.
- The CFD computations were performed using the University of Stellenbosch's Rhasatsha HPC `http://www.sun.ac.za/hpc`.

Stellenbosch University https://scholar.sun.ac.za

List of Conference Publications

Local conferences:

- N. Dumakude, 'Optimum Energy Capture and Sizing of a Stall Regulated Wind Turbine', Renewable Energy Postgraduate Symposium (REPS), University of Fort Hare, Alice, South Africa, 4-6 September 2016.

International Conferences:

- N. Dumakude, 'Validation of BEM using CFD MRF Method Coupled with Axial and Radial Induction Factors', AIAA Aviation Forum Conference on Theoretical Fluid Dynamics (TFD), Denver CO, USA, 4-9 June 2017.
- N. Dumakude and M.J. Kamper, 'Performance Evaluation of Slip Couplers with Surface- and Spoke-Mount Permanent Magnets', IEEE Energy Conversion Congress and Exposition (ECCE), Cincinnati OH, USA, 1-5 October 2017.

Awards:

- Gold Award for Best Presentation in Wind Energy. Awarded to the best student presentation in the wind energy category at the Renewable Energy Post Graduate Symposium, University of Fort Hare, Alice, South Africa, 4-6 September 2016.

Stellenbosch University https://scholar.sun.ac.za

Contents

Stellenbosch University https://scholar.sun.ac.za

Stellenbosch University https://scholar.sun.ac.za

Stellenbosch University https://scholar.sun.ac.za

Stellenbosch University https://scholar.sun.ac.za

List of Figures

Stellenbosch University https://scholar.sun.ac.za

Stellenbosch University https://scholar.sun.ac.za

Stellenbosch University https://scholar.sun.ac.za

List of Tables

Stellenbosch University https://scholar.sun.ac.za

Nomenclature

Constants

$\mu_0 = \quad 4\pi \times 10^{-7}\,\mathrm{H/m}$

Variables

Re	Reynolds number	[ ]
x, y, z	Coordinate	[m]
k	Weibull shape factor	[ ]
c	Weibull scaling factor	[ ]
ρ	Fluid density	[kg/m^3]
A	Area swept by rotor blade	[m^2]
v	Wind speed	[m/s]
P	Power	[W]
u	Wind speed	[m/s]
u_0	reference wind speed	[m/s]
α	wind shear coefficient	[ ]
m	mass	[kg]
R	raduis	[m]
a	axial induction factor	[ ]
a'	radial inductin factor	[ ]
r	spanwise position	[m]
ω	rotor angular velocity	[rad/s]
λ	tip speed ratio	[ ]
C_p	Power coefficient	[ ]
σ	standard deviation	[m/s]
$\overline{U}$	mean annual wind speed	[m/s]
I	turbulence intensity	[ ]
z_0	reference hub height	[m]
z	hub height	[m]
CF	capacity factor	[ ]

Stellenbosch University https://scholar.sun.ac.za

λ_d	d-axis flux linkage	[Wb·turns]
λ_q	q-axis flux linkage	[Wb·turns]
R	conductor resistance	[Ω]
L_d	d-axis inductance	[H]
L_q	q-axis inductance	[H]
I_d	d-axis current	[A]
I_q	q-axis current	[A]
T	induced torque	[N·m]
S	number of phases	[ ]
N_s	number of slots	[ ]
s	slip	[ ]
p	number of poles	[ ]
f	frequency	[Hz]
μ_r	relative permeability	[ ]
T	temperature	[°C]
B_r	remanent magnetic flux density	[T]
H_c	magnet coercivity	[A/m]
e	solution error	[ ]
n	iteration number	[ ]
h	magnet height	[m]
w	magnet width	[m]

Abbreviations

SCIG	Cage Induction Generator
BEM	Blade Element Momentum Theory
CFD	Computational Fluid Dynamics
NS	Navier Stokes
SA	Spalart-Allmaras
HPC	High Performance Computing
PMIG	Permanent Magnet Induction Generator
PMSG	Permanent Magnet Synchronous Generator
VSC	Voltage Source Converter
PM	Permanent Magnet
SSPMG	Slip Synchronous Permanet Magnet Generator
slip-PMC	Slip Permanent Magnet Coupler
GCC	Grid Connection Controller

Stellenbosch University https://scholar.sun.ac.za

FEM Finite Element Method
MOB Method of Bins
MLM Maximum Likelyhood Method
MM Method of Moments
AE Aero Energy
MRF Multiple Reference Frame

Stellenbosch University https://scholar.sun.ac.za

Part I

Background

Stellenbosch University https://scholar.sun.ac.za

Chapter 1

Background on Wind Energy

1.1 Introduction

Wind energy conversion systems have been used for over three millennium in grinding grain, pumping water and sailing ships. With the invention of the light bulb and the industrial revolution electrical energy generation found application in lighting buildings and supplying electric machinery. It's only in the 1940's that the first biggest electric wind turbine that generated electricity was built [6]. However, cheap oil and gas in the 1980's to early 1990s had imposed hindrance in the advancement of wind energy as a technology. Danish wind turbine manufactures in this era introduced the 'Danish concept', which is a upwind, direct-drive, stall-regulated (fixed speed) wind turbine system that uses a squirrel cage induction generator (SCIG). This was arguably to make the wind energy conversion system more cost effective in order to compete with conventional energy conversions systems of the time. Wind energy has gained traction in the recent decade due to the increase in demand for clean energy. The following sections of this chapter give a historical context into the wind modelling tools used widely in the wind industry, in order to make the reader appreciate them. These wind modelling tools are employed in this thesis.

1.2 A Word on Energy Density

Challenges faced by renewable energy systems and wind energy in particular are typically due to the energy density of these energy sources when compared to say coal or nuclear. With the energy density being defined as the amount of energy stored in a given system or region of space per unit volume, it not surprising that wind turbines would occupy more land. The power in free flowing wind is expressed by

$$P = \frac{1}{2}\rho A v^3 \tag{1.2.1}$$

Stellenbosch University https://scholar.sun.ac.za

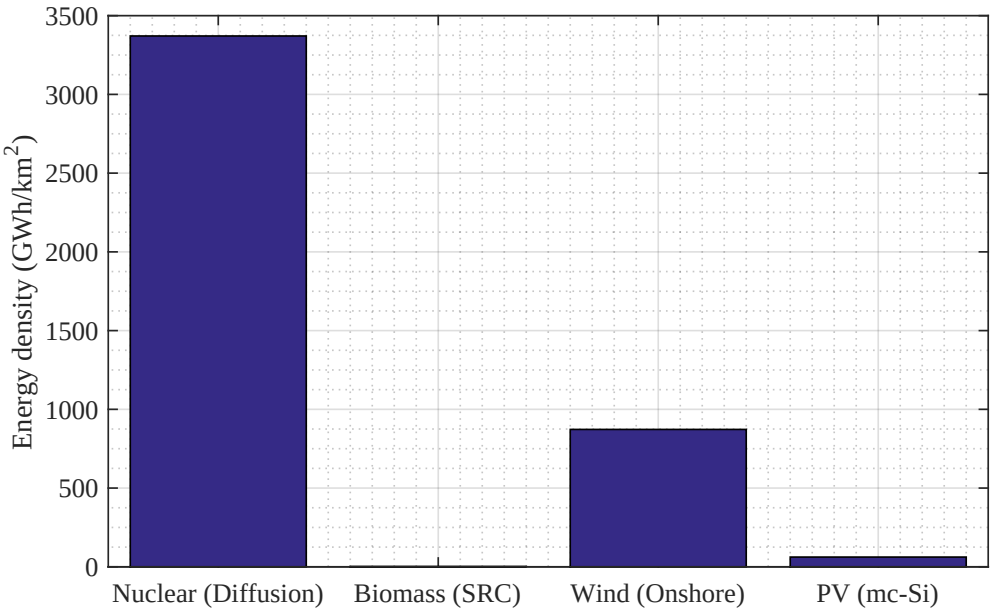

Figure 1.1: Energy density of selected sources of power generation [1].

where ρ is the wind density, A is the cross-section area swept by the wind turbine rotor and v is the free stream wind velocity. Taking the power in wind equation Eq. (1.2.1) for example, we see that power is dependent on the energy medium's density, and in order to extract energy from this medium there is an area of space taken up by the actuator that converts the kinetic energy in wind to rotational energy also known as torque. Also it might be a cultural habit that is making the adoption of renewable energy hard, as in the history of electrical energy generation the not so clean non-renewable energy sources such as coal and nuclear have been used in electrical energy generation and dominate the energy market. The data in Fig. 1.1 indicates the land-take by various energy sources, where nuclear energy generation has the smallest spatial foot print delivering more energy per unit area. Wind is second on the scale, nonetheless the land taken up by wind turbines can still be used for other purposes such as livestock or crop farming. Renewable energy doesn't require any disposal of its primary energy source that may pose an environmental threat as in the case of nuclear and fossil fuel energy sources. This is a point of departure on the pursuit of more efficient energy conversion systems particularly in the wind energy generation space.

Stellenbosch University https://scholar.sun.ac.za

1.3 BEM in Wind Energy: Historical context

The development of the blade element momentum theory (BEM) dates back to 1865 when the momentum theory was inaugurated by W.J.M Rankine for an actuator disc in marine propeller applications in 1865 [7]. Subsequent developments which followed by W. Froude (1898) who developed the blade element theory and H. Glauert (1935) who realised the complete blade element momentum theory [8], make up the core of the wind turbine modelling tool.

It is arguably the oil crisis of the 1970s that initiated the accelerated development of aerodynamic models in wind energy. In the 1980s and 1990s there was a rise of BEM codes in wind turbine design optimisations. A lot other developments since have been established and implemented, and some of these are highlighted and used in the later chapters in the wind turbine analysis of this thesis.

A comparison of Paulsen [9] field measurements with BEM and CFD for the Nordtank NTK 500/41 wind turbine performance is done in literature [10, 11], which indicates good agreement of these wind turbine models with practice. Various correction models are implemented in BEM models in order to correlate measurement to the analytical model. This renders BEM codes as hybrid models that use empirical models that are calibrated for specific flow conditions. With this said, the author greets this wind turbine modelling tool in wind turbine analysis.

1.4 CFD in Wind Energy: Historical context

Computational Fluid Dynamics (CFD) is the analysis of systems involving fluid flow by means of computer-based simulation. Its early adopter was the aerospace industry in the 1960s which started integrating CFD techniques into design, R&D and manufacture of aircraft. The severe lack of availability of affordable high performance computing hardware and computational time limitations associated with CFD solutions precluded their use. In recent years, dating back as early as the 1990s, the advances in processor speed and storage capacity of modern computers have facilitated the entry of CFD into the wider industrial community [12].

CFD is based around the concept of discretising the Navier-Stokes (NS) equations into a computational grid. This results in a large number of coupled non-linear equations that must be solved numerically. A problem of variety of scales arises in CFD, ranging from small turbulent eddies to large scales in the order of rotor diameter. A computational grid that attempts to resolve these length scale remains difficult. To overcome this challenge turbulence models are developed to model the smallest eddies. Turbulence models are

Stellenbosch University https://scholar.sun.ac.za

calibrated for various flows, and therefore their use arguably introduces additional uncertainty to the computed results. One such turbulence model is the Spalart-Allmaras (SA) turbulence model which is a one-equation mixing model that models turbulent eddy viscosity. The SA turbulence model is calibrated for external flows and is considered an adhoc turbulence model due to its simplicity, robustness and ability to yield results in a prompt manner. Another more superior turbulence model that is used for general engineering flows is the Menter k-omega shear stress transport ($k-\omega$ SST) turbulence model which is a two-equation eddy viscosity turbulence model [13]. It has the capability of switching between the standard k-epsilon ($k-\epsilon$) [14] model and the original Wilcox [15] $k-\omega$ model with the shear stress transport model that gives good results in prediction of adverse pressure gradient flows. This model is often used in turbo-machinery models and gives good results, however requires a thin mesh to resolve the boundary layer and is quite prone to instability issues especially in terms of solution convergence. Grid convergence studies make it possible to obtain a optimum solution mesh that requires fewer mesh cells but still giving accurate results, saving on computation overheads and time. With such computer based models it is possible to perform permutations on wind turbine designs which would cost a lot of time and money if done in the field. Given the availability of High Performance Computing (HPC) resources, one can pursue the use of these computation methods.

1.5 Wind Energy Conversion Systems

One of the most innovative solutions in wind energy was the 'Danish concept' which is a cost effective wind energy conversion system of its time. It uses a SCIG for converting mechanical energy due to the kinetic energy in the wind into electrical energy that can be fed into the grid. However SCIGs draw reactive power from the grid to magnetise the cage rotor, thus causing poor power factor performance on the the grid . To overcome this, SCIGs were extended with shunt capacitor banks between the stator and the grid connection for power factor compensation as shown in Fig 1.2. The permanent magnet induction generator (PMIG) is a concept that attempts to overcome the challenge posed by poor power factor performance of the conventional SCIG. This system is typically implemented in geared wind turbine systems. An-

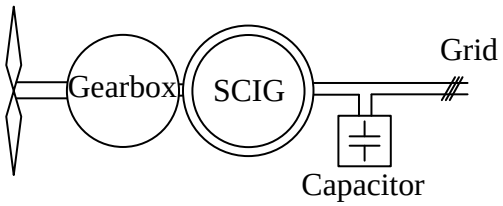

Figure 1.2: Geared SCIG system.

Stellenbosch University https://scholar.sun.ac.za

other popular non-geared type of system in wind energy generation is the the direct-drive permanent magnet synchronous generator (PMSG) shown in Fig. 1.3, with a full rated voltage source converter (VSC) that facilitates variable speed operation [16]. The generator has good power factor performance and does not require any external field excitation circuits that reduce the efficiency of the electrical generator with added field loss. Another benefit of the permanent magnet (PM) excitation is that the rotor is much lighter than that of conventional wound rotor, thus improving the torque density [17]. There are reliability and availability issues associated with geared systems, and an alternative direct-drive (gearless) system is proposed in literature [18] where the PMIG concept and the PMSG concepts are combined to form a mixed solution as shown in Fig. 1.4. This concept is called the slip-synchronous permanent magnet generator (SSPMG), which is a split system with a slip-permanent magnet coupler (slip-PMC) and a PMSG that are magnetically coupled by a freely rotating PM rotor [18, 19]. Magnetically separating the synchronous and the asynchronous machine allows the number of poles and size of the machine units to be optimally designed independent of each other [18]. The slip-PMC is directly connected to the turbine and the PMSG is connected to the grid via a grid connection controller [20]. The energy transfer occurs from the turbine rotor through the slip-PMC, PMSG and finally fed into the grid respectively. Direct-drive wind turbine generators are typically bulky and of high pole number in order to reduce the turbine rotation speed. In literature [21] different winding layouts for a surface mount PM configuration of the slip-PMC are investigated. The slip-PMC concept has proved to be implementable for wind energy applications, deriving its influence from the concept of a permanent magnet induction generator (PMIG) [22]. What is of much interest from literature is the non-overlap double layer coil layout which has shown good performance characteristic for slip-PMC machines in terms of reduced torque ripple and improved effective torque. Fig. 1.5 shows a cartoon of

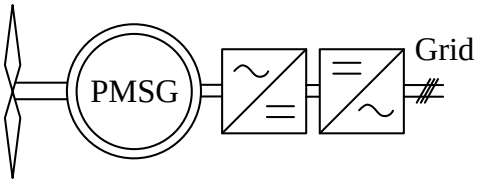

Figure 1.3: Direct-drive PMSG system.

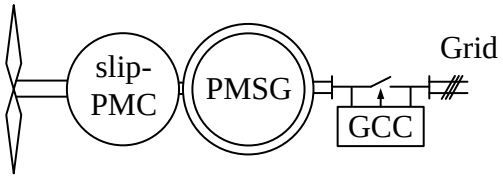

Figure 1.4: Direct-drive SSPMG system.

Stellenbosch University https://scholar.sun.ac.za

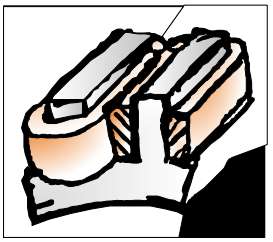

Figure 1.5: A conceptual side-by-side coil layout.

the coil layout of the slip-PMC configuration investigated in this study. The conductor windings are made from aluminum and have a high conductivity, are light in weight and a cheaper alternative to copper. It is easy to manufacture the coils using a CNC machine that cuts them out in solid rectangular shaped looped bars. The added benefit of this machine coil configuration is the high fill factor when compared to stranded coils. Each coil in Fig. 1.5 represents a phase and the number of phases and the magnetic symmetry of the electromagnetic model are determined by the chosen poles slot combination. In conjunction with the introduction of SS-PMG the analysis techniques for such a system have been developed to facilitate the design optimisation process. A multi-phase analysis model and technique procedure for slip-PMC is proposed in literature [23] which has proved to give accurate results in a computationally efficient manner. Additionally a multi-layer coil model technique is implemented that captures slot leakage effects which is information that that single-layer coil model gives little details about and in some cases neglects. With the skin effect at play especially at high frequencies a dc-to-ac resistance technique is implemented. Due to the assumptions made during the development of the analysis method in VanWyk [23], the analysis model is rendered incomplete. A fully fledged analysis technique is proposed in this thesis where the mutual, cross-coupling and field flux linkage components complete the analytical model. To the author's knowledge, only the surface-mount PM coupler shown in Fig. 8.1 is studied in literature, thus a spoke-mount PM magnet configuration shown in Fig. 8.2 is proposed in this thesis. In literature it is claimed that machine with this type of magnet orientation have a high torque density [24].

1.6 Wind Turbine System Overview

In this section a description of the proposed wind turbine system for the application of the SS-PMG system is presented. The SS-PMG is proposed for use in small-scale wind turbines, in 1-50 kW range, with a fixed speed and fixed blade pitch with stall control. Shown in Fig. 1.6 is the the complete system's visual description showing a typical setup of such a wind turbine that uses a SS-PMG for generating electrical power from wind. This wind turbine system

Stellenbosch University https://scholar.sun.ac.za

can be implemented in either a upwind or downwind configuration depending on the preferred yaw control method. The operation of this system is such that the grid is operating at a frequency of 50/60 Hz with the grid connection controller (GCC) [20] facilitating the electrical connection between the grid and the wind turbine system. The wind turbine would start-up by being driven by the wind. During this starting process the slip-PMC's wound rotor would rotate pulling the PM rotor at the same speed until the PM field rotates at synchronous speed where the PMSG's stator frequency would match with the grid frequency. As soon as the PMSG's stator frequency is synchronised with the grid frequency the grid connection controller (GCC) will switch in the wind turbine system to the grid, and the wind turbine will commence supplying energy into the grid. What controls the wind turbine's frequency is the grid frequency which governs the PMSG stator frequency.

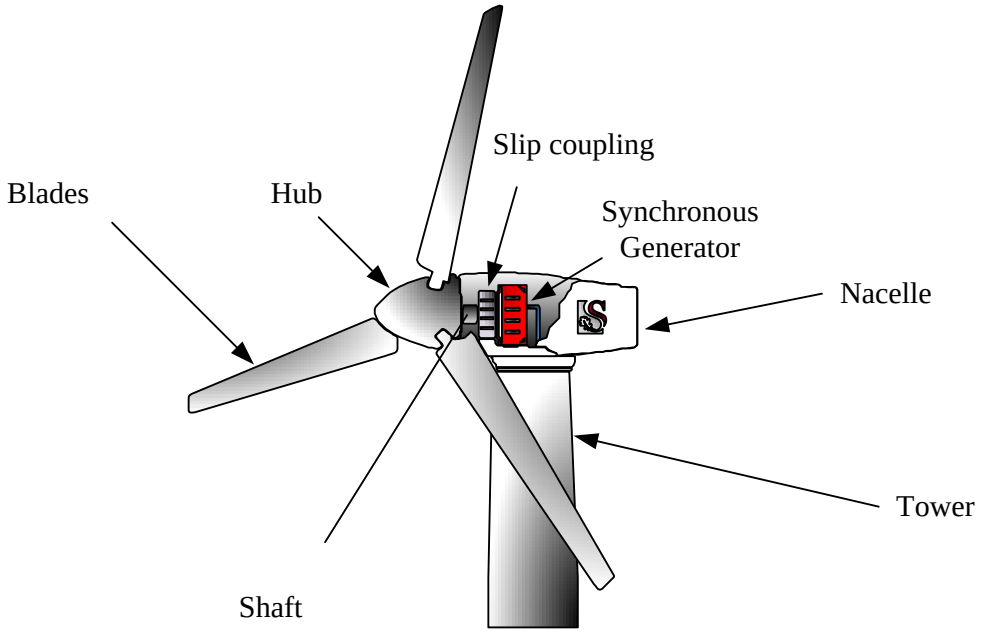

Figure 1.6: Wind turbine configuration

Stellenbosch University https://scholar.sun.ac.za

Chapter 2

Thesis Structure

2.1 Introduction

In this chapter the project motivation is given followed by the project scope and thesis layout. The author attempts to elaborate in detail as to how the thesis is structured as two aspects of energy conversion theories have been focused on, namely aerodynamics and electromagnetics.

2.2 Motivation

This project emerged about from the need of alternative slip-PMC configurations to ones already studied in literature [21, 23] in order to investigate how the variations in the structure of the slip-PMC components such as the coils and magnets affects the performance of the system. Also the analysis techniques available for such machines are still being developed on a ongoing basis in order to achieve more accurate solutions with the aid of static electromagnetic FEM methods which are considered rapid in producing solutions. The wind turbine system's aerodynamic performance has been uncertain, due to a lack of measurement off the turbine performance both in terms of torque and thrust force. It was deemed necessary to conduct a study as to how the turbine would perform using a analytical and numerical wind turbine simulator model. Another uncertainty in the aerodynamic performance of the wind turbine is under stall conditions at high wind speeds, since the wind turbine is a fixed speed and fixed blade pitch system. Although the results may differ from reality it is a good exercise to check the models in order to have a rough idea of how the turbine performance would behave under given load conditions. Also the potential gust winds are predicted to see if the mechanical and electrical components of the wind turbine can handle these extreme loads using the gust factor prediction to estimate the periods of these loads and see if these loadings are within the system's safety factor standard. A cost analysis is performed in

Stellenbosch University https://scholar.sun.ac.za

order to examine as to why small scale wind turbine systems may be expensive during uptake.

2.3 Thesis Scope

This study is limited to the preparation of the BEM, CFD and electromagnetic FEM models, implementation of these models and testing of a prototype slip-PMC aimed at evaluating the performance of the wind turbine system. Thus the focus of this research has been on:

- The development of a BEM model of the wind turbine in order to evaluate its performance under various wind load conditions.
- Develop a CFD model to verify the BEM model results in a computationally cheap manner.
- Assess the wind site characteristic, in order to determine optimum energy yield using a cost effective wind turbine configuration.
- Develop a static analytical model of the slip-PMC in order to evaluate its performance.
- Verification of the static analytical model of the slip-PMC using a dynamic commercial FEM package.
- Develop a model that would account for the skin effect experienced by the coils.
- Evaluate two slip-PMC configurations for comparison.
- Conduct a test on the laboratory test bed to validate the slip-PMC analytical model.

2.4 Thesis Layout

This thesis is structured into four parts, where in Part I the background into the study is laid out. The second part Part II discusses and characterises the aerodynamics related to the wind site and the wind turbine. A cost model of the wind turbine system is developed for a cost analysis study. Part III develops an analytical model that links with static FEM for the slip-PMC performance evaluation. Part IV concludes the thesis and recommendations are made.

The detailed layout of this manuscript is as follows:

Stellenbosch University https://scholar.sun.ac.za

- Chapter 3 characterises a given wind regime using statistical models focusing on the effects of tower height, rotor size, and extreme wind conditions.
- Chapter 4 focuses on the cost model of the wind turbine system and cost evaluation of various wind turbine configurations.
- Chapter 5 introduces the blade element momentum theory (BEM) used in the 2D wind turbine model.
- Chapter 6 describes the computational fluid dynamics model (CFD) implemented in the 3D wind turbine model used in validating the wind turbine BEM model.
- Chapter 7 presents the results from the BEM and CFD wind turbine models.
- Chapter 8 presents the development of the slip-permanent magnet coupling (slip-PMC) models.
- Chapter 9 describes the procedure of the analysis techniques.
- Chapter 10 introduces the coil impedance models that account for both the dc and ac effects.
- Chapter 11 details the bh curve characteristic of the permanent magnet (PM) and steel used in the electromagnetic FEM model of the slip-PMC and some end effects on the PM.
- Chapter 12 describes the configuration of the electromagnetic FEM model.
- Chapter 13 presents the optimisation of the slip-PMC's PM rotor in a form of a sensitivity study of the permanent magnet machine performance with a variation in the magnet dimensions.
- Appendix A details the turbulence model implemented in the CFD model.

Stellenbosch University https://scholar.sun.ac.za

Part II

Wind Turbine Aerodynamic Analysis

Stellenbosch University https://scholar.sun.ac.za

Chapter 3

Wind Analysis

3.1 Introduction

This chapter addresses the issues associated with wind turbine installations in low wind regimes, typically in urban areas. The address is in a form of a performance evaluation of different wind turbine sizes, at different hub heights, and different wind sites. The energy production optimisation is desired, particularly for wind sites with low annual wind speed averages. Typically, a low cost system is desired that outputs optimum energy in order to cost effectively generate electricity at a lowest possible cost per unit of energy.

3.2 Wind Distribution Model

The predictability of site wind speeds allow the time series wind data that appears random to be represented neatly by the Weibull probability distribution [25] which is a statistical model that represents the probability or frequency of occurrence of wind speed settings at a given site. The Weibull probability distribution is described by

$$f(v) = \frac{k}{c}\left(\frac{v}{c}\right)^{k-1} e^{-\left(\frac{v}{c}\right)^{k}} \tag{3.2.1}$$

where factors c (m/s) and k (dimensionless) are the scale and shape factor respectively. These factors are characteristic of a site's wind regime. From empirical observations in literature [26] the following is deduced:

- In normal wind regimes the scale factor c is approximately 1.1 the mean wind speed.
- A shape factor k value close to unity indicates an extremely variable wind while a k value greater than 3 ($k > 3$) indicates a more steadier wind regime.

Stellenbosch University https://scholar.sun.ac.za

The collected wind data is 10 minute mean wind speed over a period of 1 year at a hub height of 18 meters. Three methods of determining the Weibull parameters (k and c) are employed in representing the wind data, namely the method of bins (MOB), the maximum likelihood method (MLM) and the method of moments (MM) [27]. The studied wind site is a lowland site, thus it is expected to have low annual mean wind speeds when compared to a exposed site on top of a hill that might have higher annual mean wind speeds.

3.2.1 Maximum Likelihood Method

The maximum likelihood method (MLM) is a parameter estimation method that is sensitive to the Weibull k and c parameters. This way of estimating the Weibull distribution is suggested by Genc*et al* [25]. The MLM method is numerically intensive due to its iterative solution process involved in solving for the Weibull parameters. The shape factor is given by

$$k = \left(\frac{\sum_{i=1}^{n} v_i^k \ln(v_i)}{\sum_{i=1}^{n} v_i^k} - \frac{\sum_{i=1}^{n} \ln\left(v_i^k\right)}{n} \right)^{-1} \tag{3.2.2}$$

where n is the number of data samples and v_i is the ith data sample. The scale factor is given by

$$c = \left(\frac{\sum_{i=1}^{n} v_i^k}{n} \right)^{k} \tag{3.2.3}$$

3.2.2 Method of Bins

The method of bins (MOB) is another method used to represent the wind data distribution. In MOB the wind speed frequency is determined directly from the raw wind data and classed into wind speed bins. The frequency of occurrence of each wind speed within the collected wind data is determined as a probability over the whole data set. The discrete frequency distribution is given by

$$f_m = \frac{v_m}{N} = \frac{v_m}{\sum_{j=1}^{n} v_j} \tag{3.2.4}$$

where m denotes the event. The Weibull probability distribution can then be used to fit this data in a continuous manner.

3.2.3 Method of Moments

The method of moments (MM) approximates the Weibull probability distribution by using the available mean wind speed and standard deviation of the wind speed. This a rather more simple and fast method of approximating the Weibull distribution especially for large data sample sizes [25]. The k and c problem in the MM is solved by determining the mean wind speed given by

Stellenbosch University https://scholar.sun.ac.za

Eq. (3.2.7) and the standard deviation given by Eq. (3.2.8). The gamma function $\Gamma(1+\frac{1}{k})$ in Eq. (3.2.6) is determined using a numerical solver such as Matlab. The shape factor is given by

$$k = \left(\frac{\sigma}{\overline{U}}\right)^{-1.086} \tag{3.2.5}$$

where σ is the standard deviation and $\overline{U}$ is the data mean wind speed. The scale factor is given by

$$c = \frac{\overline{U}}{\Gamma(1+\frac{1}{k})} \tag{3.2.6}$$

where $\overline{U}$ is the mean wind speed, $\Gamma(1+\frac{1}{k})$ is the Gamma function and k is the scale factor. The mean wind speed is determined by

$$\overline{U} = \frac{1}{n}\sum_{i=1}^{n} v_i \tag{3.2.7}$$

where n is the data sample size and v_i is the ith wind data sample. The standard deviation is determined by

$$\sigma = \frac{1}{n-1}\sum_{i=1}^{n}\left(v_i - \overline{U}\right)^2 \tag{3.2.8}$$

3.3 Collected Wind Data Statistics

The wind data is collected on a location in Stellenbosch called Mariendahl, which is the University of Stellenbosch wind turbine technology test facility. Shown in Fig. 3.1a is the raw 10 min average wind speed data recorded at the wind site. The recorded peak 10 min average wind speed is approximately 16.22 m/s. This raw data is then processed using the statistical methods presented in the previous sections to yield the plots shown in Fig. 3.1b. The wind data statistics are as follows:

- The annual mean wind speed is

$$\overline{U} = 4.0293 \text{ m/s} \tag{3.3.1}$$

- and the standard deviation is

$$\sigma = 2.5997 \text{ m/s} \tag{3.3.2}$$

The annual mean wind speed from the wind site is actually quite low. The standard deviation is approximately 55% of the annual mean wind speed which indicates a high variability in the annual wind speeds and thus the wind may

Stellenbosch University https://scholar.sun.ac.za

Table 3.1: Weibull data fit parameters

	MLM	MM
k	1.6294	1.6094
c	4.5257	4.4965

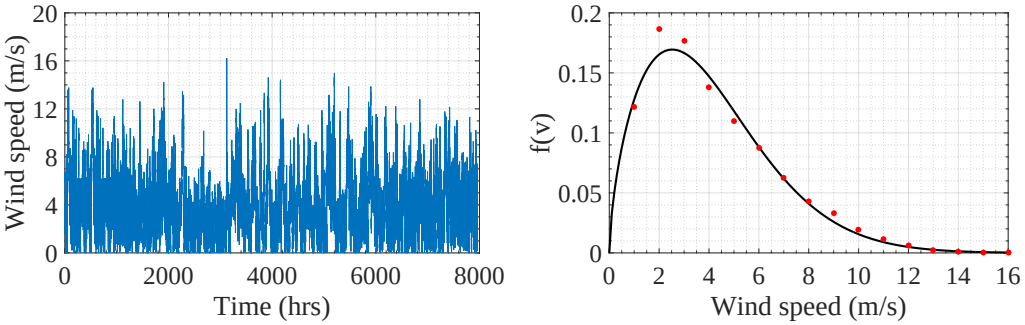

(a) (b)

Figure 3.1: Wind site characteristic with (a) the raw wind speed data time series and (b) the Weibull distribution fit of the raw wind data representation

.

be very turbulent, due to the terrain.

A summary of the data fitting parameters of the Weibull probability distribution are given in Table 3.1. From the analysis of the data it is concluded that the MLM fits the data more accurately, due to its iterative nature, that is based on a optimisation procedure that minimises the error between the actual data and the curve that fits the data [27], thus the MLM method is used in fitting the wind data and the MM method is used in determining the standard deviation and mean wind speed of the data. Clearly from Fig. 3.1b the most frequent wind speeds are far low and typical cut-in wind speeds of wind turbines are $3-4$ m/s. However in this study it is assumed that these wind speeds are acceptable and that the cut-in wind speed is the approximately 1 m/s.

3.4 Wind Gusts and Turbulence

Turbulence in wind is typically considered to be wind speed fluctuations on a fast time-scale in the time range less than 10 minutes [28]. These fluctuations carry high energy and are filtered out by the 10 min average wind speed sampling process. The turbulence intensity is a measure of the overall level of turbulence. It is defined as

$$I_u = \frac{\sigma}{\overline{U}} \tag{3.4.1}$$

Stellenbosch University https://scholar.sun.ac.za

where σ is the standard deviation of the wind speed variation about the mean wind speed $\overline{U}$, usually defined over 10 min or 1 h.
The gust factor G, which is a measure of the ratio of the gust wind to the mean wind speed, can be used in estimating the maximum wind gust at any given time interval. The time interval gust factor is given by

$$G(t) = 1 + 0.42 I_u \cdot \ln \frac{3600}{t} \tag{3.4.2}$$

which is an expression for the ratio of the gust wind to the hourly mean wind speed, where I_u is the longitudinal turbulence intensity. This expression is then adapted for the annual mean wind speed and used in determining the time interval mean gust. Expression (3.4.2) is propoesed in literature [28] and Wieringa [29] shows consistency of this model with experimental results.The gust factor model also makes it possible to de-construct the data to find the 10 min annual gust factor and even an estimate of the 1s time interval gust factor which can be considered to be a component of turbulence. The gust wind is calculated as follows

$$U_{\text{gust}} = G(t)\overline{U} \tag{3.4.3}$$

where $\overline{U}$ is the annual mean wind speed. The cut-out wind speed of 16 m/s is justified by the 10 min annual gust given by Table 3.2 which correlates with the recorded 16.2 m/s 10 min mean wind speed shown in Fig. 3.1a. A turbulence intensity of $I_{\text{u}} = 0.6452$ is obtained, which is quite high indicating the high variability of the winds at this particular site.
The 1s wind gust given in Table 3.2 is representative of the usually stormy winds which are typical of the region. The short bursts of wind gusts could possibly be absorbed by the system inertia. It is desirable to determine the

Gust period	1s	60s	5min	10min
U_{gust} (m/s)	22.88	18.41	16.65	15.90

Table 3.2: Wind gust data based on the gust factor model for turbulence intensity of $I_{\text{u}} = 0.6452$.

time it takes for a certain extreme wind condition to persist before it dies out. One could translate this to a time unit of hours, minutes and seconds. Since as per convention, machinery safety factors allow operation at 2 times the system rated power for a average operation time of 5 minutes. The system protection is important to ensure safe and reliable operation of the system. The wind can also assist in cooling the system and hence improving the system performance. One can look for a five minute time interval and constrain the wind turbine operation to this maximum time duration under extreme wind load conditions.

High moment of inertia could assist in absorbing the high torque pulses induced by the wind gust. The system electrical rating is 10 kW, however the

Stellenbosch University https://scholar.sun.ac.za

Gust period	U_{gust} (m/s)	P_{load} (W)	F_{load} (N)
1s	22.88	13 540	2 926
60s	18.41	11 869	2 243

Table 3.3: Wind gust loading on the wind turbine system components.

wind turbine analysis data gives peak power of 11 518 kW at wind speed of 13 m/s. According to IEC 61400, small wind turbine generator system's safety factor requirements are as given in Table 3.4. According to most electrical ma-

Load determination method	Safety factor for fatigue loads	Safety factor for ultimate loads
Simple load calculation	1.0	3.0
Aero-elastic modelling with design data (rpm, power)	1.0	1.35
Load measurement with extrapolation	1.0	3.0

Table 3.4: Partial safety factors for loads IEC61400-2 [5].

chines manufacturers, to avoid excessive rotor heating the maximum torque must be at least 1.4 times the rated torque, (40% higher than the load torque) However given the machine current density in the machine under rated conditions and breakout torque conditions the current is well below the condition where excessive heating detrimental to the machine insulation is reached.

3.5 Wind Regime Variability

The wind site wind resource characteristic determines the amount of energy available in the wind. It is engineers task to design wind turbines that produce optimum energy subject to environmental constraints. Two wind regimes are introduced for comparison in order to evaluate the wind turbine potential at different wind regimes. The actual wind site resource called site 1, is where the wind turbine will be erected. The fictitious wind site called site 2, is a theoretical wind regime that is deemed ideal for the wind turbine. The shape factor (k) for the fictitious wind site is chosen such that the average annual wind speed is near the wind turbine's maximum efficiency, in effect illuminating the wind turbine rotor's potential energy harvest. The wind turbine rotor evaluated in this section is the Aero Energy (AE) turbine with 3.6 m long blades, with three blades. The capacity factor is a measure of how effective a

Stellenbosch University https://scholar.sun.ac.za

wind turbine is performing at a given wind site. It is defined as follows

$$capacity\ factor = \frac{average\ power}{rated\ power} \tag{3.5.1}$$

where the average power is determined by annual energy production of the wind turbine on a specific site and the rated power is the installed generator rating. In Fig. 3.2a the wind distribution of the two wind sites is shown, where site 2 demonstrates high average annual wind speed when compared to site 1. The energy production from site 2 shown in Fig. 3.2b is outstanding for the same installed capacity as site 1. So it is quite obvious that given you have separate users in site 1 and site 2, that site 2 reaps substantial benefits when compared to a user at site 1. Site 1, as indicated by its low shape factor value ($k = 1.63$) in Table 3.1, is turbulent due to the terrain that is surrounded by mountains and hills with a little bit of shrub. Site 2 is assumed to be steady in order to give a bell curve or Gaussian distribution. Again Fig. 3.2c indicates a high capacity factor for the wind turbine at optimum wind turbine rotation where maximum energy harvest is achieved. So after all there is such a thing as a good wind site and a bad wind site. This shows how well the wind turbine performance can be depending on the wind site characteristic.

3.6 Impact of Tower Height

The wind turbine tower is one of the most substantial components, as it accounts for about 31% of the total cost of most small scale wind turbine installations [2]. It is desired to keep this component cost as low as possible. So an investigation is launched as to how the energy production is affected by increasing the hub height from 18 m to 50 m. The power law is applied in order to adjust the wind speed from the recorded reference data to desired hub height. The power law is given by

$$u = u_0 \left(\frac{z}{z_0}\right)^{\alpha} \tag{3.6.1}$$

where u_0 and z_0 are the reference wind velocity and hub height. The exponent $\alpha = 0.16$ is the wind shear coefficient that is derived empirically and whose value is dependent on wind site terrain. The surface roughness height is assumed as $z_0 = .03$ of roughness class 1, which is characteristic of open agricultural terrain. Generally, the closer the hub height to the surface roughness height, the more turbulent or disturbed the flow gets. In Fig. 3.3a the energy production of the wind turbine at a hub height of 50 m is shown, where clearly the increase in optimum energy production is observed to be 49.35% that of hub height 18 m. The capacity factor shown in Fig. 3.3b indicates marginal increase from that of hub height of 18 m. However the increase in hub height may pose a high cost on the wind turbine total cost. A higher increase in

Stellenbosch University https://scholar.sun.ac.za

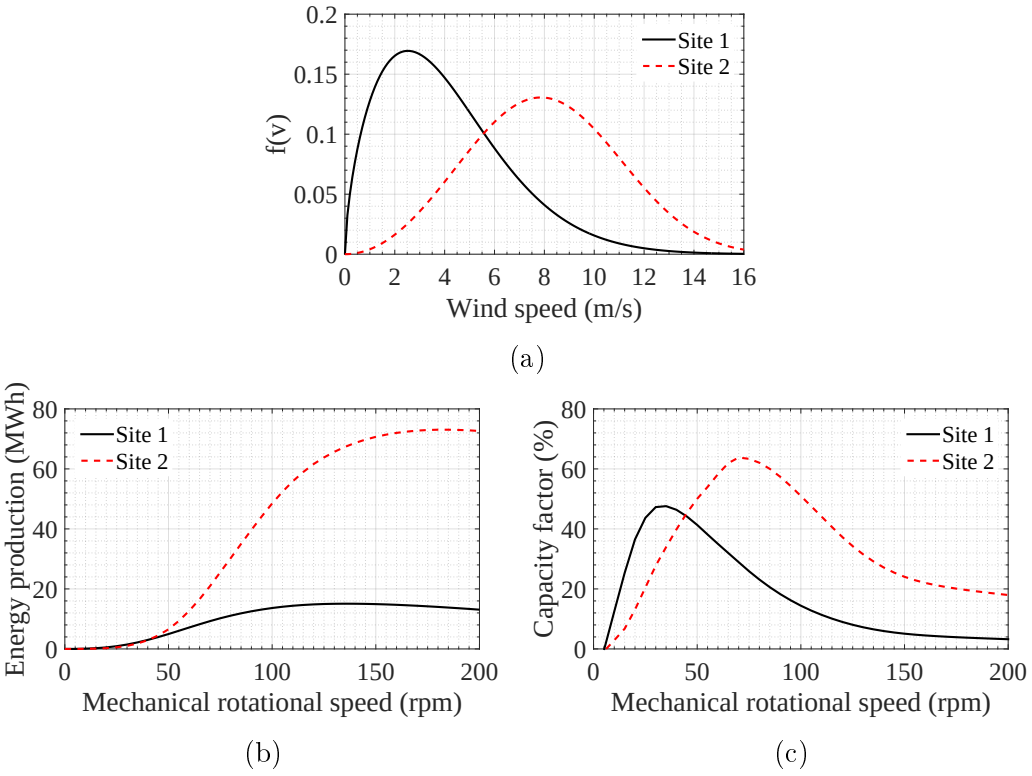

Figure 3.2: Wind regime variability (a) is the wind distribution, (b) is the annual energy production and (c) is the capacity factor of the wind sites, with the installed Aero Energy (AE) turbine.

capacity factor could be achieved with the fictitious wind regime of §3.5 in Fig. 3.2a, but then again this is not realisable.

3.7 Wind Turbine Rotor Size

The wind turbine rotor size selection greatly determines the overall drive train size. A choice of three wind turbine blade sizes are evaluated on how they would influence the wind turbine's overall efficiency. These turbine blades are selected due to the availability of their design information in the public domain and their differences in size which may be considered to be in the small scale range. In Fig. 3.4a the SERI-8 [30] wind turbine performance appears to give high energy production. It is a 3 bladed turbine rotor that is 8.55 m in radius which is quite large and might require to be erected on a higher hub height other than 18 m. The NREL Phase VI wind turbine rotor is 5.55 m in radius, and is a two bladed rotor. Fig. 3.4b indicates that overall the Aero Energy (AE) 3.6 wind turbine, which is a 3 bladed rotor, performs well in terms of the capacity factor. Which is suggestive that small scale wind turbines perform well in low wind regime sites, given that they operate at high rotational speeds.

Stellenbosch University https://scholar.sun.ac.za

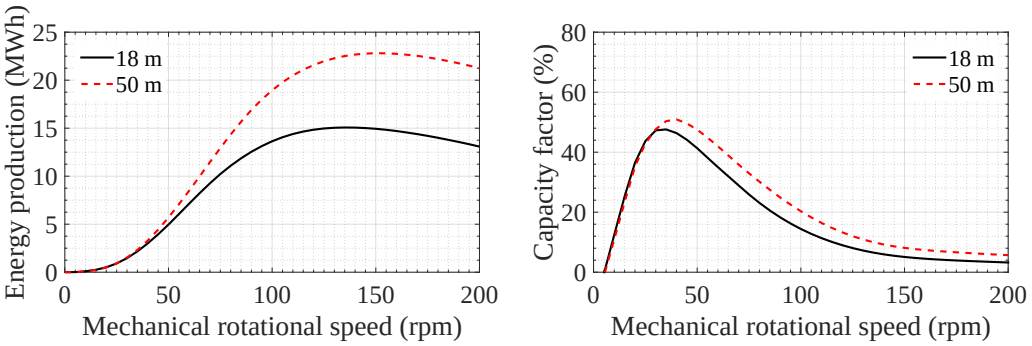

(a) (b)

Figure 3.3: Wind turbine hub height variation with (a) energy production and (b) the capacity factor

.

The capacity factor reflects on the cost of the wind turbine system, and the lower it is, the higher the price.

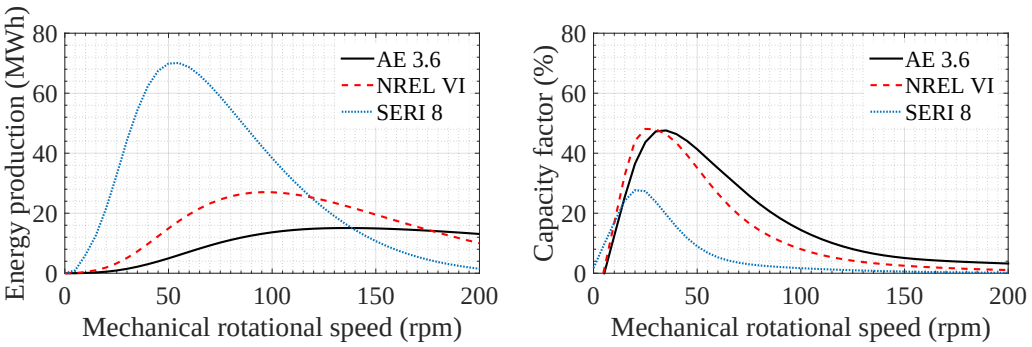

(a) (b)

Figure 3.4: Various wind turbine rotor size's (a) annual energy production and (b) capacity factor at a fixed height and wind regime.

3.8 Summary

Statistical models used in the recorded wind data analysis are introduced, where MLM is used to fit the MOB data which is representative of the raw data. The MM is used to determine the mean annual wind speeds and the standard deviation of the annual wind speeds from the annual mean wind speed. The wind data characteristic exhibits that of a low wind site. Gust winds are reconstructed from the 10 min mean wind speed data recorded, using a gust factor model. The gust factor model has shown to reproduce the recorded maximum 10 min mean wind speed and that it also gave an indication

Stellenbosch University https://scholar.sun.ac.za

of the gust persisting for shorter time frames. Given the design safety factor and time constant of the wind turbine, the operation under these gusts is deemed bearable only if they persist for short periods not exceeding the safety factor period which is typically 5-10 min at double the rated power. The effect of wind regime are demonstrated by comparing wind turbine performance at an existing wind site and a fictitious wind site, highlighting the potential of the wind turbine and how it is limited in a low wind regime site.
The wind turbine rotor size performance comparison is performed in order to optimise the energy production taking into account the capacity factor for small-scale wind turbines.
The impact of tower height is also investigated taking care as to mind the cost of the wind turbine tower.

Stellenbosch University https://scholar.sun.ac.za

Chapter 4

Wind Turbine Cost Analysis

4.1 Introduction

This chapter introduces the problem of wind turbine drive train components sizing and how this affects the cost of the wind turbine system. Potential solutions to minimise the cost are proposed.
There are a number of different ways to measure cost, and each way brings about its own insights. Only the equipment cost is examined, namely the turbine blades and electrical generator cost for small-scale wind turbines. Financing costs, total installed cost, fixed and variable O&M costs, etc are not considered in this manuscript. However the results presented in this thesis serve as indicators as to how these costs are impacted. The initial capital cost of small-scale wind turbines is generally high due to the size of the small-scale wind energy market being small even though fuel costs are zero due to the wind being free. Transparency in the cost modelling of such system is imperative, in order to highlight potential areas of savings and in effect minimise the cost of the initial capital investment that goes in to small-scale wind energy systems in development to improve the attractiveness of such systems. The main variables that greatly affect cost, such as wind turbine rotor size and the energy conversion sub-systems that pose knock-on effects are investigated. The cost analysis presented in the subsequent section is a simple cost analysis that uses general trends in conventional machine manufacture costs. These trends are subject to change due to market volatility.

4.2 Wind Turbine Cost Breakdown

The small-scale wind turbine cost breakdown presented in Fig. 4.1 is as adapted from [2]. The most dominant components in the cost pie chart are the turbine and tower. The wind turbine is the most critical at a given height in terms of energy harvest. The tower is a passive component, involved in the adjustment of the mean annual wind speed. The gain in the increase in mean

Stellenbosch University https://scholar.sun.ac.za

annual wind speed with tower height is site dependent, and in some cases may not provide satisfactory results, especially if the wind site is of low wind speed nature. The manipulation of the wind turbine rotor size and hence electric generator, seems more cost effective to obtained the desired energy harvest at a minimum cost. With such data it is possible to estimate the cost of the rest of the wind turbine system, given that one knows one of the component cost in advance.

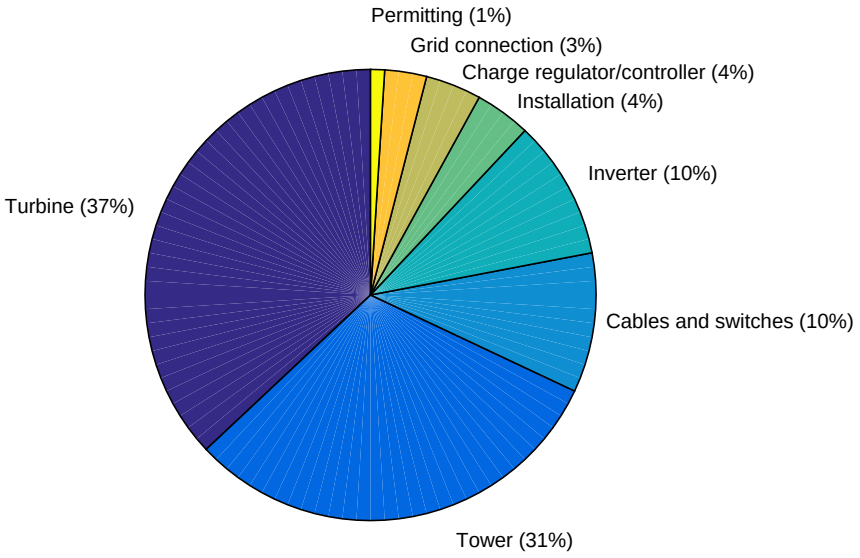

Figure 4.1: Pole mounted small-scale wind turbine components cost breakdown chart [2].

4.3 Blade Mass and Cost Estimation

The blade mass increases by approximately the power of three of the blade length: $m_{\text{blade}} \propto R^3_{\text{blade}}$. Consequently the output power would increase by the power of two of the blade length: $P \propto R^2_{\text{blade}}$, which clearly demonstrates the influence of wind turbine rotor diameter on power production. The blade mass is given by:

$$m_{\text{blade}} = 1.7R^{2.3} \tag{4.3.1}$$

where R is the rotor radius. This blade mass model is an empirical model derived by Guido [31] from experimental results from Tembra GmbH's wind turbine rotor inventory. We assume that the blades are manufactured from fiberglass and epoxy for the shell and spars or webs for a hollow structure and stuffed with foam in the interior. The density of fiberglass is assumed to be $\rho_{\text{epoxy}} = 1500$ kg/m^3 and that of PVC foam is $\rho_{\text{foam}} = 200$ kg/m^3.

Stellenbosch University https://scholar.sun.ac.za

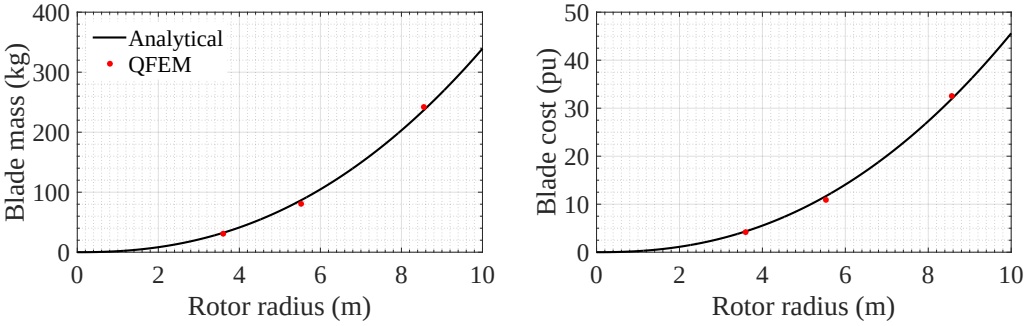

(a) (b)

Figure 4.2: (a) Blade mass versus rotor radius from(4.3.1) and QFEM, (b) Blade cost estimation with rotor size with base cost of $307.69.

QFEM [32] which is discussed in Lennie [33], is used in calculating the blade mass, and Eq. (4.3.1) is used to analytically estimate the blade mass. The solution from QFEM and those given by Eq. (4.3.1) are in agreement for the wind turbine blade cases investigated in this chapter. There appears to be an exponential correlation between the blade mass and rotor radius as stated by Eq. (4.3.1). It is assumed that the exponential correlation of the blade mass with rotor radius is directly proportional to that of the blade cost in order to model the cost of the turbine rotor with its size. The blade mass determined using QFEM and the analytical blade mass model Eq. (4.3.1) are shown in Fig. 4.2a which indicate a good correlation. The blade cost is determined using a base cost ($) per mass (kg) where the baseline blade cost is estimated as $307.69 for small scale wind turbines.

4.4 SSPMG Mass and Cost Estimation

Assume that the mass of a conventional machine ready for operation to be the same as that of the synchronous generator of small-scale wind turbine generator of the same power rating in development. A sample of machine ratings with their corresponding mass and cost were collected to establish the plot shown in Fig. 4.3. These graphs give an estimate of trend values of the wind turbine electrical machine components, using electrical machine manufacturers cost data scaled for the system type introduced in this thesis. These may be used to benchmark small-scale wind turbine manufacturers' claims.
The cost of the slip-synchronous permanent magnet generator (SSPMG) which is introduced in Part I is split into discrete cost packages for transparency in cost variability. This may serve as useful information for clients of wind turbine manufacturers who would buy the system components separately. An observation from the data is that there is a linear correlation in generator

Stellenbosch University https://scholar.sun.ac.za

mass, cost and generator power or torque when assuming the highest possible machine pole number and keeping it as high as possible for direct drive wind turbines.

4.5 SSPMG Cost Modelling

For systems that consist of parts that can be modelled separately and built separately it is desired that the system components cost be determined individually, should a client want to purchase the wind turbine parts separately as replacement parts. The sum total cost of the slip-PMC and PMSG of the wind turbine is estimated by

$$C(x) = \kappa(1+\beta)C_{\mathrm{B}}(x) \tag{4.5.1}$$

where $C(x)$ and $C_{\mathrm{B}}(x)$ are the wind generator cost and the baseline cost when the design parameter takes on value x which in this case is the wind turbine rated power. κ is the number of generator parts, i.e. in this case the PMSG and slip-PMC, thus $\kappa = 2$, and β is the proportion of the cost that depends on product development stage, ease of manufacture or manufacture complexity, costs, size, etc. One can say that β is a measure of development effort required in developing new designs. In this study it is assumed that $\beta = 0.9$ indicating that the machine is still in development phase i.e. the machine is not mass produced in a factory or assembly line. The latter statement is valid since, the SSPMG technology is a concept that is still in its infancy, and has many more years to go in development. To separate the cost of the wind generator parts, assume some mass ratio of slip-PMC and PMSG mass. With this assumption one is able to calculate the cost of the slip-PMC and PMSG respectively as follows:

$$C_1(x) = k_1 C(x) \tag{4.5.2}$$

$$C_2(x) = k_2 C(x) \tag{4.5.3}$$

where by definition

$$k \equiv \frac{m}{m_t}, \tag{4.5.4}$$

m is the component mass, and m_t is the system total mass. In this manuscript $k_1 = 0.413$ and $k_2 = 0.586$ based on design optimization results obtained in Potgieter [19] and VanWyk [34] for component mass. Assume that the total mass is directly related to the mass of the complete generator mass. Obviously the market price is subject to inflation and will dictate the gradient of the cost plot as well as the number of subcomponents in the system (κ) and development stage of the machine (β). The observed trend is linear in nature, as shown in Fig. 4.3.

Stellenbosch University https://scholar.sun.ac.za

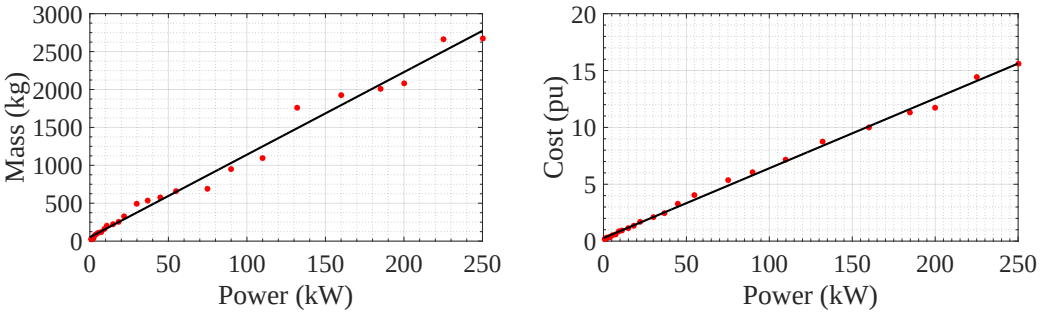

(a) (b)

Figure 4.3: Wind turbine slip synchronous generator: (a) mass vs rated power and (b) cost vs rated power where the base cost is $ 7 692.31 (R100k).

4.6 Drive Train Cost Evaluation

Two wind turbine rotors of different number of blades and size are evaluated, namely the NREL Phase VI and the Aero Energy wind turbine, neglecting the SERI-8 in this case. A summary of the wind turbine performance for the cases considered in §3.7 is presented in Table 4.1. The best performing turbine system in terms of energy production and wind turbine efficiency is the NREL Phase VI wind turbine operating at $n = 50$ rpm, mounted at a hub height of 18 m. The energy from this wind turbine system is enough to supply approximately 5 households per annum. With the benefit of a high capacity factor, this means that the overall system drive train cost is reduced and thus cheaper yielding higher returns on investment. With the lower wind turbine rotation speed, this adds positively to the environmental friendliness of the wind turbine, as lower rotational speeds generally have lower noise pollution on the environment.

Increasing the hub height from 18 m to 50 m results in an increase in energy production of approximately $\approx 39.24\%$ and an increase in the capacity factor of about 43.03%. The price increase with tower height will probably off-set the gain in energy production and thus the cost of electricity. This cost does not affect the nacelle components cost significantly, however we avoid this cost analysis due to scope constraints.

The mass of the wind turbine components is given in Table 4.2 to demonstrate how each component contributes to the tower top (nacelle) mass. It is desired to minimise the nacelle mass, and the Aero Energy wind turbine seems to give the lowest nacelle mass of 219.88 kg at a hub height of 50 m. This however, may not be the best, since the tower mass increases with height and as was stated earlier tower mass modelling is out of scope. Operating at 100 rpm as given Table 4.1 would be an another ideal alternative, however, the

Stellenbosch University https://scholar.sun.ac.za

energy production and turbine efficiency is much lower. With an addition of 4.36% in tower top mass of that of the Aero Energy wind turbine, the NREL Phase VI turbine at 18 m takes the cake. However, a general observation is made in terms of the deviation of mass in the wind turbine components, that is determined by the turbine rotor size and desired output power for direct drive systems. These results highlight that for small scale wind turbines in low wind regimes, installing larger turbine rotors gives better energy yield and capacity factor.

The cost of the systems are comparable to each other, the advantage of the one system over the other is the cost involved in long term operation of the turbines, in maintenance. The system with a low capacity factor will be more expensive to maintain when compared to a high capacity factor system. This is blatantly the result of the more costly components for a small energy yield. The cost per annual energy harvest is not considered here given that there are variables such as the hub, grid connection costs, installation costs, etc. which are not considered and which will have an impact on the overall cost.

	P_{rated} (kW)	AEP (kWh)	CF (%)	n (rpm)
NREL Phase VI	4.6	15 100	35.12	50
AE	10.7	13 727	14.41	100
AE @ 50m	6.4	15 784	28.02	85

Table 4.1: Rated power matrix of wind turbine components.

	B_{mass} (kg)	N_{bladde}	C_{mass} (kg)	G_{mass} (kg)	T_{mass} (kg)
NREL VI	88.45	2	41.7	59.44	278.04
AE	32.93	3	69.15	98.48	266.42
AE @ 50m	32.93	3	49.94	71.15	219.88

Table 4.2: Mass matrix of wind turbine components.

	B_{cost} (pu)	C_{cost} (pu)	G_{cost} (pu)	t_{cost} (pu)
NREL VI	0.935	0.225	0.326	1.486
AE	0.522	0.378	0.542	1.442
AE @ 50m	0.522	0.271	0.391	1.184

Table 4.3: Cost matrix of wind turbine components.

Stellenbosch University https://scholar.sun.ac.za

4.7 Summary

The wind turbine cost breakdown for small-scale systems is presented highlighting the potential areas of saving. The blade mass and cost model are presented to facilitate the cost analysis of the turbine cost with size. The cost modelling of the SSPMG machine is done in order to separate the cost of the subsystem components and to have a more transparent cost outline of the machine. This cost proves to be accurate in estimating the cost of the SSPMG system given that it is in early developmental phase. The drive train cost evaluation asses the cost of the wind turbine configuration that is considered to yield optimal energy production at a cost effective price.

Stellenbosch University https://scholar.sun.ac.za

Chapter 5

BEM Wind Turbine Model

5.1 Introduction

Low cost wind turbine simulations in R&D are achieved by using the BEM theory approach that yields results more rapidly during the design process of wind turbines. This two-dimensional method assumes steady state input aerodynamic lookup tables of the lift and drag coefficients. These lookup tables are created using codes such XFOIL [35], where the angles of attack are limited in range. Originally XFOIL was designed for the analysis of aircraft wings, since aircraft designers do not desire stall, aircraft wings operate under low angles of attack. To facilitate the use of these lookup tables in wind energy and especially for stall controlled wind turbines, Montgomery [36] developed an extrapolation technique that extends the lift and drag angle-of-attack range. Additionally the Himmelskamp effect corrects for the 3D effect, where in stalled or separated flow the Centrifugal and Coriolis forces are dominant, thus altering the 2D lift and drag coefficient characteristic.
In 2D the wind turbine blade is discretised into turbine airfoil cross-sections, which in the analysis are assumed to be of infinite span length. To account for a finite blade length, the Prandtl tip loss model corrects this assumption. Due to viscosity effects the drag curve is modified to account for Reynolds effects, for various flow conditions, since the input lift and drag vs angle of attack data tables are generated for specific Reynolds numbers.

5.2 Governing Equations

The actuator disc theory is employed in analytically modeling the fluid flow around a rotor disc which creates a stream-tube that separates the region of the fluid that is affected by the actuator disc from the free stream flow velocity. In this formulation the mass flow rate is assumed the same everywhere along

Stellenbosch University https://scholar.sun.ac.za

the stream-tube, from far upstream, at the disc and the wake, which implies

$$\rho A_\infty U_\infty = \rho A_d U_d = \rho A_w U_w. \tag{5.2.1}$$

The Bernoulli equation, which can be derived from the Navier-Stokes equations, is given by

$$\frac{1}{2}\rho U^2 + p = \text{constant}. \tag{5.2.2}$$

Applying Bernoulli's equation Eq. (5.2.2) in (5.2.1) from far upstream to just before the actuator disc and from just behind the disc to far downstream, and using some mathematical manipulation the axial induction factor which models the change in axial velocity and hence change in momentum is obtained. The flow velocity at the rotor plane is described by

$$U_d = (1 - a)U_\infty \tag{5.2.3}$$

and the wake flow velocity is given by

$$U_w = (1 - 2a)U_\infty \tag{5.2.4}$$

where a is the axial induction factor which models the flow velocity deficit. From Eq. (5.2.3) and (5.2.4) we arrive at a linear interpolation of the flow velocity at the rotor plane which is given by

$$U_d = \frac{1}{2}(U_\infty + U_w). \tag{5.2.5}$$

To account for rotation effects, the wind turbine is considered as a rotor without a stator [28], the wake rotation direction is noted to be opposite that of the rotor due to the reaction torque. The induced angular velocity at the rotor disc is given by $a'\Omega$. The wake angular velocity just after the rotor disc is given by $2a'\Omega$. The radial induction factor is defined as

$$a' = \frac{\omega}{2\Omega} \tag{5.2.6}$$

where ω is the wake angular velocity and Ω is the rotor angular velocity. From the one dimensional momentum theory the following optimum relation between the radial induction factor and the axial induction factor is established [28]

$$a' = \frac{1 - 3a}{4a - 1}. \tag{5.2.7}$$

The axial and radial induction factors in the BEM algorithm are determined iteratively using

$$a = \frac{1}{\dfrac{4\sin^2\phi}{\sigma C_n} + 1} \tag{5.2.8}$$

Stellenbosch University https://scholar.sun.ac.za

and

$$a' = \frac{1}{\frac{4\sin\phi\cos\phi}{\sigma C_t} - 1} \tag{5.2.9}$$

respectively. The BEM method relies on 2D lift and drag versus angle of attack input data tables, like that shown in Fig. 5.1b. This data is generated in XFOIL [35] for each airfoil section along the turbine blade span. This data is then extrapolated for higher angles of attack using the Montgomerie extrapolation technique in [32] which is discussed in detail in [36]. The Himmelskamp effect is accounted for automatically by the solver, where as a rule of thumb the Himmelskamp is effective in high rotor angular velocities [36].

5.3 Performance Equations

The induced torque on the turbine rotor is given by the integral of

$$dM = \frac{1}{2}\rho B \frac{U_\infty(1-a)\Omega r(1+a')}{\sin\phi\cos\phi} c C_t r dr \tag{5.3.1}$$

where ρ is the fluid density, B is the number of rotor blades, U_∞ is the freestream velocity, Ω is the rotor angular velocity, r is the spanwise distance from the turbine root, a' is the radial induction factor, a is the axial induction factor, c is the chord length, C_t is the tangential coefficient, ϕ is the angle of incidence with respect to the rotor plane. The induced thrust is given by

$$dT = \frac{1}{2}\rho B \frac{V_\infty^2(1-a)^2}{\sin^2\phi} c C_n dr \tag{5.3.2}$$

where C_n is the normal coefficient.

5.4 Reynolds Number

Reynolds number is used in predicting or characterising the behaviour of air flow around an airfoil i.e., whether flow is laminar or turbulent. Reynolds number is characteristic of body size and flow velocity. Two forces are considered by the Reynolds number formulation, namely inertial forces on the numerator and the viscous forces on the denominator. Inertial forces are due to the flow of the fluid such that the fluid particles interact with high enough kinetic energy promoting turbulent flow. Viscosity is a quantity that describes how thick is a fluid and viscous forces are in a form of friction promoting laminar flow. The lift and drag behaviour of airfoils is Reynolds number dependent, such that the behaviour at one Reynolds number may not be valid for another Reynolds number [37]. Reynolds number is given by

$$\mathrm{R_N} = \frac{\rho c|V|}{\mu} \tag{5.4.1}$$

Stellenbosch University https://scholar.sun.ac.za

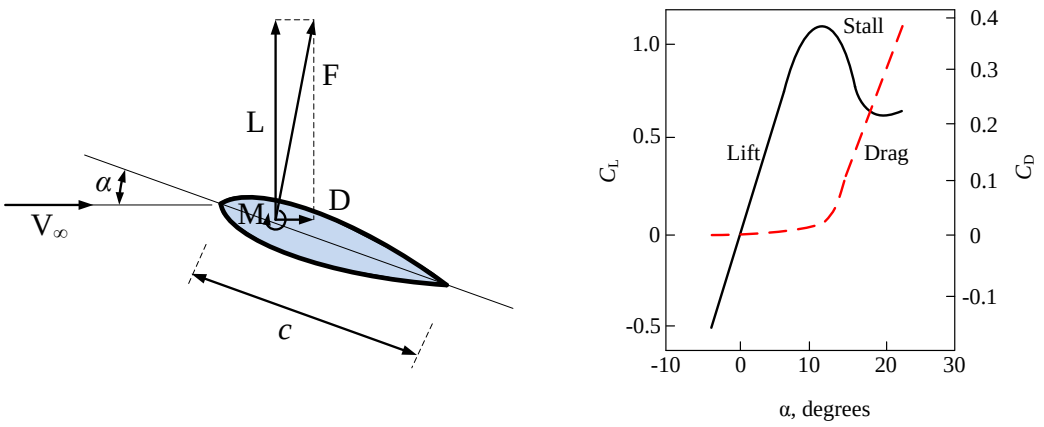

(a) (b)

Figure 5.1: 5.1a Airfoil lift and drag definition and 5.1b Airfoil lift and drag definition [3].

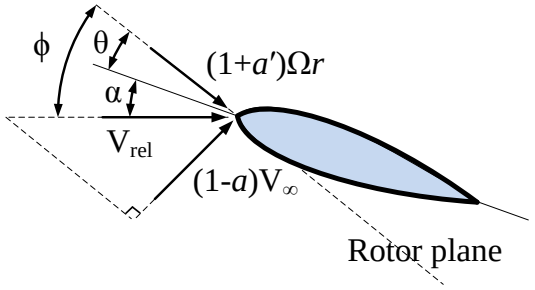

Figure 5.2: Flow velocity definition for rotating airfoil section [3]

where ρ is the air density, c is the chord length, $|V|$ is the absolute flow velocity, and μ is the air viscosity. The flow velocity is assumed to be

$$|V| = \sqrt{(V_\infty^2 + V_{\text{tip}}^2)} \tag{5.4.2}$$

where V_∞ is the free stream flow velocity and V_{tip} is the blade tip velocity. Assuming free wind gusts of up to a maximum of 30 m/s and tip speed of up to a maximum of 75 m/s. The direction of the incoming wind velocity is accounted for by reporting the data as a function of the angle-of-attack given as

$$\alpha = \arctan\left(\frac{V_\infty}{V_{\text{tip}}}\right) \tag{5.4.3}$$

The angle-of-attack assists in estimating the max angle-of-attack to use in airfoil parameter estimation such as lift and drag coefficient curves.
It is assumed that the maximum speed of the incoming air flow, including the rotor blade tips speed, is less than the speed of sound i.e. Mach=0.3. This deems the flow incompressible.

Stellenbosch University https://scholar.sun.ac.za

5.5 2-D Aerodynamics

Wind turbines use the lift force induced on the blades to drive the rotor. Lift is normal to the incident velocity V_∞ as shown in Fig. 5.1a and drag is the force induced on the turbine blades that is along the streamwise direction. This drag force is largely responsible for the so called thrust force on the wind turbine. Lift and drag coefficients C_l and C_d are defined as:

$$C_{\mathrm{L}} = \frac{L}{1/2\rho V_\infty^2 c} \tag{5.5.1}$$

and

$$C_{\mathrm{D}} = \frac{D}{1/2\rho V_\infty^2 c} \tag{5.5.2}$$

where ρ is the air density and c is the length of the airfoil, often denoted by the chord. The unit for the lift and drag in equation Eq. (5.5.1) and (5.5.2) is force per length (N/m). A chord line can be defined as the line from the trailing edge to the nose of the airfoil. Airfoil analysis codes such the Drela XFOIL [35] are used in obtaining the lift and drag versus angle of attack look up tables. The lift and drag curves presented in Fig. 5.3 are for the SG6040, which is one of the airfoil profiles recommended for wind turbines blades [38]. This profile is used at the root of the blade since it has a thick camber which gives a good lift characteristic at low flow velocities. Fig. 5.3a is obtained from the 2-D airfoil analysis tool XFOIL, illustrating the limitation of the data to only low angles of attack. The Montgomerie [36] extrapolation technique that extends the 2-D airfoil polars for high angles of attack is used in achieving the data shown in Fig. 5.3b.

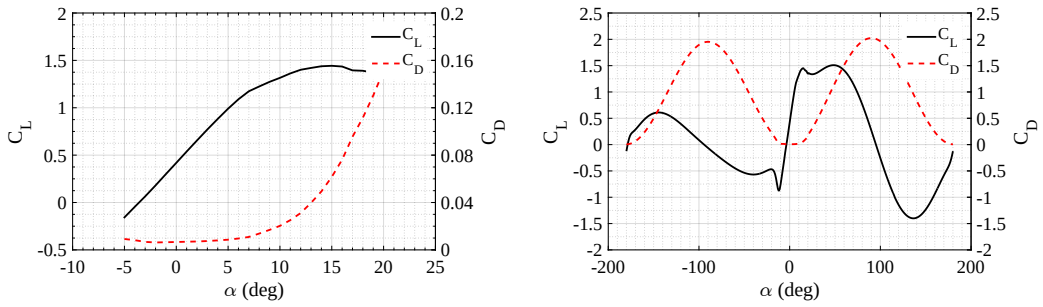

Figure 5.3: (a) Unextrapolated lift and drag coefficients as derived from XFOIL and (b) Extrapolated lift and drag coefficients as derived from the Montgomerie extraplation method [3]

Stellenbosch University https://scholar.sun.ac.za

5.6 BEM Analysis Procedure

First the design of the wind turbine blade airfoil shapes is performed and the airfoil coordinates are imported into XFOIL. One does this for each airfoil type used in modelling the wind turbine blade cross-sections. Then the chord length is specified for each airfoil station. The local flow Reynolds number is determined using the Reynolds number equation and the local flow conditions on a given airfoil station. The polar plot of the angle-of-attack versus lift/-drag is simulated for the allowable angles of attack. The polar plot is then extrapolated with the Montgomerie extrapolation technique for a 360° range of angle of attack lift and drag data. Then the wind turbine blade is created in QBlade [32] by placing the airfoil sections at their respective stations, specifying their position along the span length, the airfoil type, Reynolds number, blade local twist angle, and chord length. The number of blades is specified for wind turbine simulation, wind speed range i.e. cut-in and cut-out wind speeds, wind viscosity, air density, tip- and root loss models, and 3D correction model. For power regulation and speed control a fixed blade pitch control and fixed-speed control for transmission is specified.

5.7 Summary

The BEM theory for wind turbine modelling is illustrated. Where special correction models such as the the Himmelskamp that corrects for 3D effects, Prandtl loss model that corrects for a finite number of blades, and the Reynolds effect that affects the lift and drag input data obtained from XFOIL. The XFOIL lift, drag data is angle of attack limited and thus the Montgomery extrapolation technique extends this data for higher angles of attack.

Stellenbosch University https://scholar.sun.ac.za

Chapter 6

CFD Wind Turbine Model

6.1 Introduction

Computational Fluid Dynamics (CFD) models in wind energy are treated as close to experimental data in the absence of experimental data. This assumption is arguably justified by the fact that turbulence models in fluid dynamics are often calibrated for various flow conditions [12]. The fully resolved wind turbine rotor model approach is often used in validating the wind turbine analytical model (BEM). In literature [39, 40], good consistency among experimentation, CFD and BEM is demonstrated. The global loads such as power and thrust force are typically of interest to wind turbine designers. It is proposed, in order to aid the process of obtaining a correlation between BEM and CFD, that the actuator disc theory be implemented in determining the approximate axial induction factor from the CFD simulation to compare the axial and radial induction factor based on input flow angular velocity and the probed simulation output velocity data near the turbine blades of the two wind turbine simulation methods. These radial and axial induction factors are then used to account for the wake rotation. Hence the relative angular velocity between the rotor and the wake is specified as the input angular velocity to drive the CFD simulation. This phenomenon seems not to be captured well by the multiple reference frame (MRF) model if only the rotor angular velocity is considered. The MRF method is known to model best rotor-stator problems where the two system components do not strongly interact with each other, in other words where there is little or no wake rotation and examples of these flows are turbo machinery in enclosures where wakes and their losses are not resolved since they are deemed negligible.

Stellenbosch University https://scholar.sun.ac.za

6.2 Governing Equations

The wind flow problem is assumed to be best represented by the incompressible Navier-Stokes equation

$$\boldsymbol{\nabla} \cdot (\rho \mathbf{u} \cdot \mathbf{u}) = -\boldsymbol{\nabla} p + \boldsymbol{\nabla} \cdot (\mu \boldsymbol{\nabla} \mathbf{u}) \tag{6.2.1}$$

where p, ρ, μ denote the pressure, density, and dynamic viscosity, respectively. The MRF technique is employed in the steady state simulation, that solves the Navier-Stokes equations in a relative frame

$$\boldsymbol{\nabla} \cdot (\rho \mathbf{u}_r \cdot \mathbf{u}_r) + 2\rho \boldsymbol{\Omega} \times \mathbf{u}_r + \rho \boldsymbol{\Omega} \times \boldsymbol{\Omega} \times \mathbf{r} = -\boldsymbol{\nabla} p + \boldsymbol{\nabla} \cdot (\mu \boldsymbol{\nabla} \mathbf{u}_r) \tag{6.2.2}$$

The relative velocity u_r is defined by

$$\mathbf{u}_r = \mathbf{u} - \boldsymbol{\Omega} \times \mathbf{r} \tag{6.2.3}$$

where $\boldsymbol{\Omega}$ is the angular velocity. The Coriolis acceleration in this formulation is represented by $2\boldsymbol{\Omega} \times \boldsymbol{u}_r$ and the centrifugal forces are captured by $\boldsymbol{\Omega} \times \boldsymbol{\Omega} \times \boldsymbol{r}$.

6.3 Performance Equations

The total surface force acting on the control surface is given by

$$\sum \boldsymbol{F}_{\text{surface}} = \int_{CS} \sigma_{ij} \cdot \boldsymbol{n} dA \tag{6.3.1}$$

where σ_{ij} is the stress tensor, $\boldsymbol{n}$ is the surface normal vector dA is the differential surface element. The stress tensor is defined as follows

$$\sigma_{ij} = \begin{pmatrix} \sigma_{xx} & \sigma_{xy} & \sigma_{xz} \\ \sigma_{yx} & \sigma_{yy} & \sigma_{yz} \\ \sigma_{zx} & \sigma_{zy} & \sigma_{zz} \end{pmatrix} \tag{6.3.2}$$

where the diagonal components of the stress tensor are called normal stresses, which constitute pressure, and the off-diagonal components are called shear stresses, which make up the viscous stresses. Hence, the surface force equation may be decomposed and written as

$$\sum \boldsymbol{F}_{\text{surface}} = \sum \boldsymbol{F}_{\text{pressure}} + \sum \boldsymbol{F}_{\text{viscous}} \tag{6.3.3}$$

The moment on the control surface is given by

$$\sum \boldsymbol{M}_{\text{surface}} = \int_{CS} \boldsymbol{r} \times \sigma_{ij} \cdot \boldsymbol{n} dA \tag{6.3.4}$$

where $\boldsymbol{r}$ is the vector location of the point of action of the force. Again, the moment can be decomposed into pressure and viscous moment components as follows

$$\sum \boldsymbol{M}_{\text{surface}} = \sum \boldsymbol{M}_{\text{pressure}} + \sum \boldsymbol{M}_{\text{viscous}} \tag{6.3.5}$$

Stellenbosch University https://scholar.sun.ac.za

6.4 Convergence

Two convergence criteria are employed in this study, as each one brings about different insight about the flow fields' stability and consistency with the grid. The computation grid is mostly dense on the surface of the actuator body, namely the turbine rotor and the MRF cell zone. A refinement on body surface mesh shows a substantial solution improvement. The computation grid extent is such that the wake behind the turbine rotor is enough to allow stabilisation of the flow. The criteria used to monitor convergence are the residuals given by the software package which are a measure of continuity or conservation of the flow properties and the key global body moments and forces. These are shown in Fig 6.1b and 6.1c where equilibrium of the global fields is clearly reached after 300 number of iterations and 800 iterations for the residuals as shown in Fig. 6.1a demonstrating solution stability. An attempt to improve solution convergence had been implemented by performing mesh independence studies and selecting appropriate turbulence models and numerical schemes etc. The analysis is allowed to reach convergence by allowing the solution to run through enough iterations such that any numerical diffusion is detected if it ever occurs. The numerical solution is as good as the mesh and boundary conditions specified in the problem.

The probed flow velocity in the CFD simulation is near the turbine blade surface at about $r/R = 55.55\%$ of the rotor span. Table 6.1 gives the probed velocities given by $U = \sqrt{U_x^2 + U_y^2 + U_z^2}$ for each flow condition and the corresponding axial and radial induction factors with the aid of the theory presented in §5.2. From this table the axial induction factors calculated based on the rotor's input parameter which is the radial induction factor agrees well with the flow's axial velocity output from the simulation velocity field results.

Table 6.1: CFD Flow Parameters from 1-D Momentum Theory [3]

U_∞	U	$a' = \frac{\omega}{2\Omega}$	$a = \frac{1+a'}{4a'+3}$	$a = 1 - \frac{U}{U_\infty}$
7	4.82	0.5	0.3	0.311
8	5.48	0.6190	0.2956	0.3156
11	7.54	0.8095	0.290	0.314
16	11.58	0.5238	0.299	0.276

Stellenbosch University https://scholar.sun.ac.za

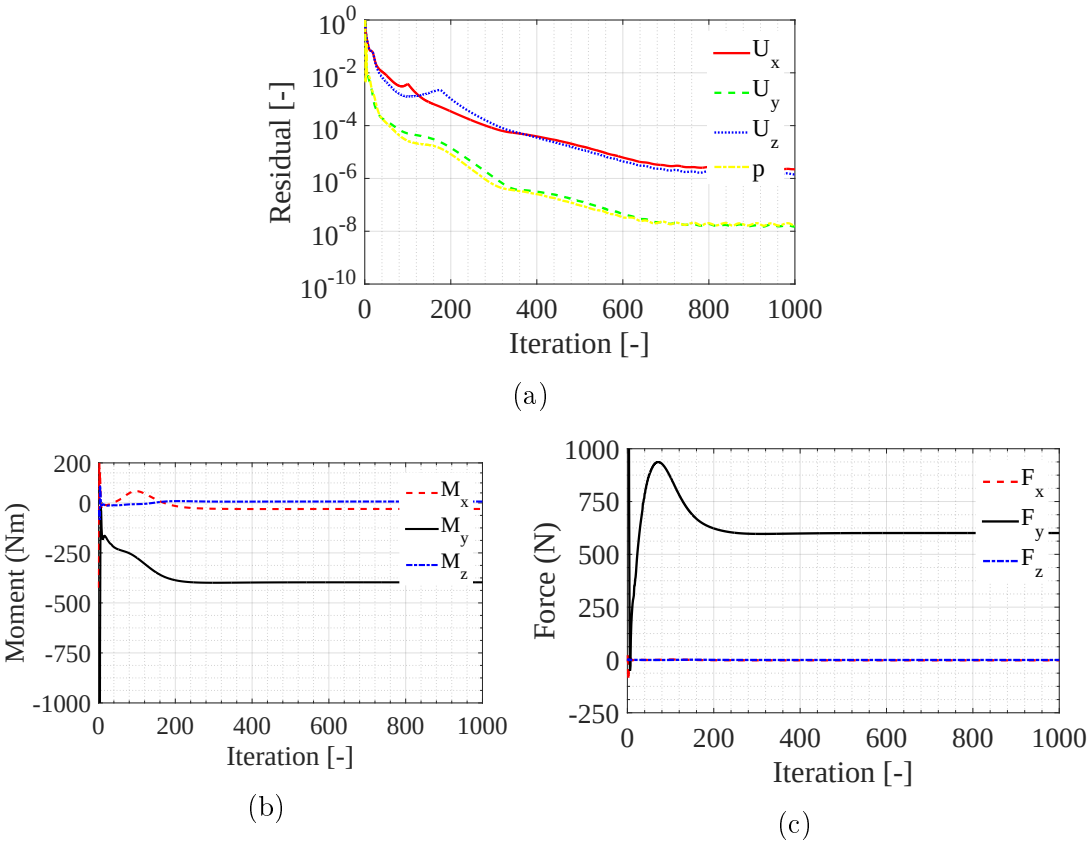

Figure 6.1: (a) CFD simulation residual levels [3], (b) Simulation results torque convergence rate, (c) Simulation results force convergence rate of a fully converged simulation.

6.5 Turbulence Model

The Semi-Implicit Method for Pressure-Linked Equations (SIMPLE) algorithm is employed for steady state simulation with the Spalart-Allmaras (SA) turbulence model. The SA is a one-equation mixing length model by Spalart-Allmaras, which models the turbulent eddy-viscosity. In appendix A is the SA turbulence model detailing the relationship between the turbulent viscosity and the modified turbulent viscosity. This turbulence model is considered numerically stiff when compared to the Menter $k-\omega$ SST turbulence model [41]. It has a high convergence rate and works well on relatively coarse grids which is ideal for rapid solutions using modest available computation resources. The SA turbulence model is calibrated for external flow thereby reducing any uncertainty introduced by turbulence models and in [42] it has shown to give good results for flows across airfoils. In order to analytically model the boundary layer the '`nutUSpaldingWallFunction`' in OpenFOAM is used to resolve the boundary layer along the turbine rotor surfaces eliminating the need to resolve the boundary layer with a very thin mesh which is expensive.

Stellenbosch University https://scholar.sun.ac.za

6.6 Meshing

The computation domain is shown in Fig. 4 where the static background mesh dimensions are determined with respect to the MRF region disc diameter to ensure that the boundaries don't affect the convergence and stability of the flow solution. The background mesh is generated using OpenFOAM's `blockMesh` which is a structured background mesh generator. Mesh grading on the static background mesh is $20 \times 20 \times 20$ cells along the x-, y- and z-axis. OpenFOAM's

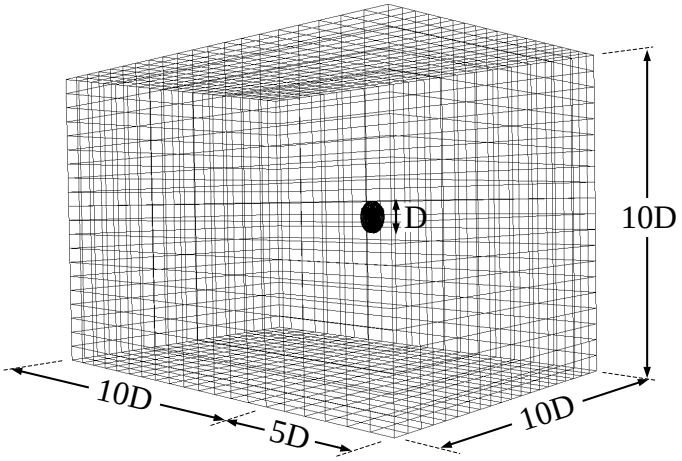

Figure 6.2: Computation domain mesh [3]

'`snappyHexMesh`' which is a mesh generator is used in generating a cell zone mesh for the MRF region and the wind turbine rotor surface mesh. In Fig. 6.3a and 6.3b the wind turbine surface mesh is shown to illustrate the mesh quality by the leading and trailing edge on one of the turbine blades, which intersects the hub by the root of the blade. The wind turbine blade surface mesh refinement level is `(11 11)` and the hub surface mesh refinement level is

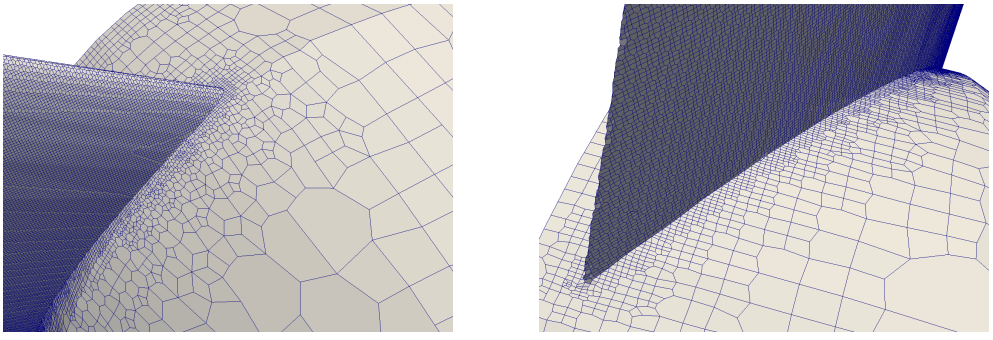

(a) (b)

Figure 6.3: (a) Blade leading edge mesh quality, (b) Blade trailing edge mesh quality [3].

Stellenbosch University https://scholar.sun.ac.za

`(2 9)`. The total grid size is approximately 7.2M cells, which is the medium mesh (M2) achieved during the grid convergence test. The mesh settings are presented in §6.7.

6.7 Mesh Sensitivity Test

The mesh independence test is performed in order to optimize the computation domain for the best possible accuracy using minimal computation resources and time. The solution convergence is monitored during the mesh independence procedure to verify the solution convergence. The parameters used as indicators of convergence are k the transport equation, p, U_x, U_y, and U_z the continuity quantities and the wind turbine performance solution convergence such as the moments and forces. The mesh independence procedure is as follows:

1. Size the computation domain extent big enough such that it encloses the wind turbine and MRF region. Typically downstream along the flow direction, one would make the extent of the field long enough to allow the wake enough room to stabilize. Run the solution convergence test.

2. Up-size or down-size the computation domain grid spacing by factor 2 and perform another solution convergence test. If the solution convergence is not met in the down-sized case, then up-size the computation domain and the other way around. The solution tolerance or error must be small enough to justify the mesh resolution.

3. Once the optimal mesh is reached the grid cell size (mesh resolution) must be determined. This is generally calculated and the solution convergence test is repeated here.

In the end the following computation domain size was selected, with D denoting the actuator diameter:

- the length of the computation domain downwind is set ten times the diameter of the actuator (10D)

- the length of the computation domain upwind is set five times the diameter of the actuator (5D)

- the width of the computation domain is set to five times the diameter of the actuator (5D)

- the height of the computation domain is set to five times the diameter of the actuator (5D)

Stellenbosch University https://scholar.sun.ac.za

A visual description of the computation domain dimensions is given in Fig. 6.2. The solver tolerance is set such that the maximum tolerance level is reached, where the solution is deemed sufficiently accurate. After the mesh sensitivity test was complete a summary of the results is given in Table 6.2 and their corresponding settings in Table 6.3. During the meshing process most of the cells are generated during the castellated mesh refinement for the MRF cell zone and the surface mesh generation. The meshing time indicates this, where the computational fluid domain is refined and doesn't have much of an effect on the meshing time as given in Table 6.2. However a refinement in the surface mesh has a tremendous influence on the meshing time. The refinement in both the surface and fluid domain mesh has the same effect on the solution time. With the coarse mesh (M1) the solution is close enough to the benchmark result obtained from the BEM simulation.

Table 6.2: CFD mesh independence statistics

	Coarse (M1)	Medium (M2)	Fine (M3)
Mesh size (-)	837 744	7 226 624	16 433 906
Parallel processors (-)	48	48	48
Meshing time (hrs:min:s)	0:00:32	0:17:09	0:17:07
Solver time (hrs:min:s)	0:17:52	3:24:29	8:15:59
Iterations (-)	1000	1000	1000
Moment (Nm)	372.91	397.03	391.50
Thrust (N)	787.43	600.90	628.83

Table 6.3: CFD mesh settings statistics

	Coarse (M1)	Medium (M2)	Fine (M3)
`blockMesh`	20 20 20	20 20 20	40 40 40
`snappyHexMesh` blade surface	9 9	11 11	11 11
`snappyHexMesh` hub surface	2 9	2 9	2 9
`snappyHexMesh` MRF	1 4	1 4	1 4

6.8 Boundary and Initial Conditions

The simulation case directory is `windTurbine`, which consists of `0`, `const`, and `system`, and some command files for the preparation of the case directory, execution of mesh generators and solvers. Four files are contained in the `0` sub-directory namely `p`, `U`, `nut` and `nuTilda`, which are case files referred to as dictionary files where the flow fields boundary conditions are prescribed. The

Stellenbosch University https://scholar.sun.ac.za

pressure is static and the flow is incompressible. In this section the details of the boundary conditions and the initial conditions will be outlined.

6.8.1 Velocity (U)

The velocity file `U` is used in prescribing the boundary conditions and initial values of the velocity field at the inlet, outlet, top, bottom, left, right and wall patches. The inlet velocity is of '`type fixedValue`' with a uniform value for an even velocity distribution. At the outlet a '`type inletOutlet`' condition is specified where the solver determines the outlet velocity condition accounting for any backflow. At the wall a '`type movingWallVelocity`' is specified with a zero absolute velocity.

6.8.2 Pressure (p)

A '`type zeroGradient`' with a value of '`uniform 0`' is set at the inlet implying that the inlet pressure is a atmospheric pressure. Similarly at the outlet a static pressure condition is prescribed. For the wall boundary, a '`type zeroGradient`' is set at the wall, implying that there is no field quantity penetrating the wall boundary. For the top, bottom, left, and right patches or boundaries, '`type slip`' boundaries are set that enforce the flow field to conform to the free stream conditions.

6.8.3 Turbulent viscosity (nut)

Given the uncertainty of the turbulent viscosity at the inlet and outlet a '`type calculated`' boundary condition is prescribed where the turbulent viscosity is determined based on the flow conditions. The wall boundary is of '`type nutkWallFunction`' where the turbulent viscosity is determined analytically. The side boundaries are of '`type slip`'.

6.8.4 Modified viscosity (nuTilda)

For the viscosity like transport property a `type fixedValue` is prescribed at the inlet with some prescribed value. The outlet is of `type zeroGradient`. The wall is of '`type fixedValue`' with a '`value uniform 0`' and the side boundaries are of '`type slip`'.

6.8.5 Fluid properties (transportProperties)

Since the flow is incompressible, the solution is independent of the fluid density (ρ), it is not necessary to specify it. The kinematic viscosity is prescribed with a value of $\nu = 1.4833e^{-5}$ m^2/s.

Stellenbosch University https://scholar.sun.ac.za

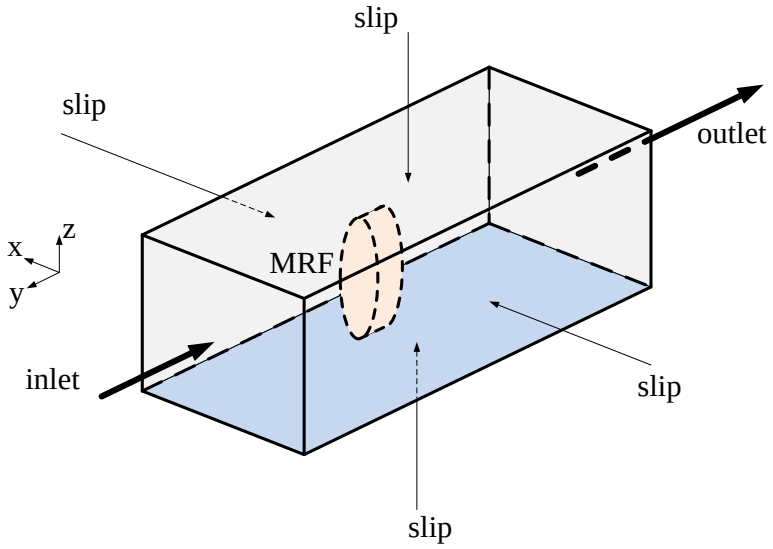

Figure 6.4: CFD model computation domain boundary

6.9 CFD Analysis Procedure

The wind turbine is first modelled using the BEM code QBlade as explained in §5.6 to establish baseline power and thrust data. A CFD fully resolved rotor model is developed to validate the BEM results by employing the 1-D momentum theory, which is introduced in §5.2, to calculate the axial and radial induction factor of the CFD flow model to obtain consistency between the two methods using the concepts presented in §5.2. In other words the CFD flow model is probed at the rotor plane for the flow velocity and the freestream flow velocity and the result thereof is used to calculate the axial induction factor using Eq. (5.2.3). The flow is probed by means of the `probes` function in OpenFOAM. The radial induction factor is then determined by using Eq. (5.2.7) which is also given by Eq.(5.2.6) by considering the wake and rotor angular velocity. In the CFD simulation inputs we use the wake angular velocity ω, as it appears from Eq. (5.2.6) that the relative rotation angular velocity between the rotor and the wake is not accounted for in this equation. In this study, since the frozen rotor concept is employed which implies that the flow around the turbine is rotating, thus the relative angular velocity between the wake and the rotor in a dynamic case is accounted as the wake rotation in the static case given by $(1+a')\Omega = \omega$. The author also notes that the velocity deficit in CFD is modeled by the velocity deformation terms of velocity spatial gradients. The numerical scheme used to perform some linear interpolation on the flow velocity is similar to that of momentum method in Eq. (5.2.5). This is one of the similarities that BEM and CFD share in common and thus would enforce consistency between the two methods especially in flow modeling around wind turbines.

Stellenbosch University https://scholar.sun.ac.za

6.10 Summary

The CFD model is introduced, whereby the Navier-Stokes equations for stationary and rotating region of flow are presented. The performance evaluation models are presented, highlighting the surface stresses on the turbine rotor contribute to the turbine performance. The selected convergence criteria is presented where the convergence parameters considered are shown to converge within the allocated number of iterations. The one dimension momentum model indicates good agreement between the CFD probed flow parameters and the BEM flow parameters using the optimum relationship. The turbulence model used is the Spalart-Allmaras turbulence model due to its robustness, numerical stiffness and fast convergence rate. Wall function is used in modelling the boundary layer in order to avoid using a thin mesh which expensive. The meshing tools used are presented, namely snappyHexMesh and blockMesh generator. Mesh domain size is presented. A mesh sensitivity is performed where a medium mesh that yielded accurate results at a minimum computation resource cost is selected for the rest of the operating points performance analysis. The boundary and initial conditions which greatly influence the CFD results are presented for a more comprehensive illustration of the flow behaviour at various boundaries of the flow domain.

Stellenbosch University https://scholar.sun.ac.za

Chapter 7

Wind Turbine Performance

The analysis of the wind turbine rotor performance is done to see how the turbine would respond under given conditions. With this theoretical data the wind turbine drive train is designed with this in mind. It is important to have all the data necessary in the drive train design, such as loading on the support structure, drive train components, and blades.

7.1 Power and Thrust Curve

The power and thrust curve are computed for the wind turbine running as a stall controlled machine as shown in Fig. 7.1. The power curve of the two methods is in agreement. The thrust curve also demonstrates consistency between the CFD and BEM results, although there appears to be a marginal difference especially below stall. This discrepancy in the thrust curve is attributed to the analytical thrust model Eq. (5.3.2) that appears to not account for the rotation effect as the radial induction factor (a') and the rotor angular velocity (Ω) do not appear in the thrust equation. Yet, if these results are close to reality, this would mean good news, as low loading on the tower would be experienced. And the agreement in deep stall is due to the breakdown of BEM for axial induction factors greater than 0.4 where the analytical model is discarded and the Glauert empirical model extrapolates the thrust coefficient. Again, if this is true and close enough to reality, it would prove how accurate CFD is from reality, given the model is empirical.

7.2 Power Coefficient, Cp

The wind turbine rotor power coefficient is defined as the power extracted by the wind turbine relative to that available in the free wind stream. It is a measure of the aerodynamic efficiency of the wind turbine rotor blades.

$$C_p = \frac{P_{\text{extracted}}}{P_{\text{available}}} \tag{7.2.1}$$

Stellenbosch University https://scholar.sun.ac.za

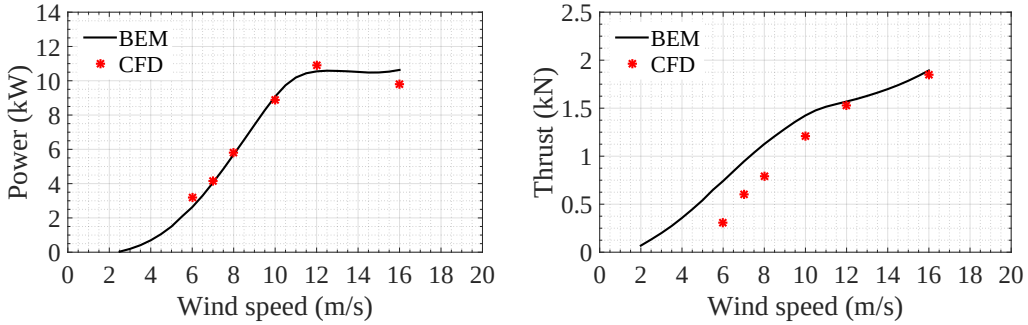

(a) (b)

Figure 7.1: (a) Computed power curve and (b) Computed thrust curve [3] of the Aero Energy blade at a fixed rotational speed of 100 rpm.

The maximum achievable energy power efficiency is 59% which is known as the Betz limit. The limit is not caused by any deficiency in design but by the physics [43]. The tip speed ratio is given by

$$\lambda = \frac{\text{speed of rotor tip}}{\text{wind speed}} = \frac{\omega R}{U_0}, \tag{7.2.2}$$

where Ω is the rotor angular velocity, R is the rotor tip radius and U_0 is the free stream wind velocity. Generally a high tip speed ratio is desirable since this is where the wind turbine rotor operates aerodynamically most efficiently. The aerodynamic efficiency of the rotor can be expressed as a function of the tips speed ratio $C(\lambda)$, as shown in Fig. 7.2. A maximum aerodynamic efficiency of approximately $C_p = 0.47$ is achieved at a tip speed ration of $\lambda = 6.5$ as shown in Fig. 7.2. The lower aerodynamic efficiencies at lower tip speed ratios are desirable for stall regulated wind turbines rotors, where the excess energy from the wind is shed to prevent overloading the turbine electrical components in high wind speeds.

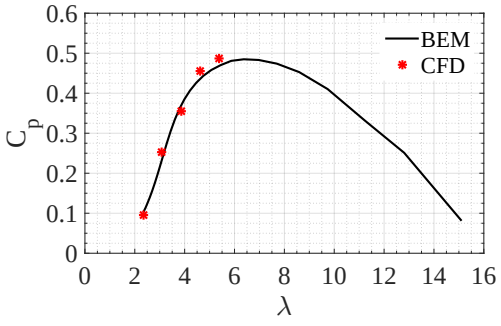

Figure 7.2: Wind turbine rotor C_p curve of the Aero Energy blade.

Stellenbosch University https://scholar.sun.ac.za

7.3 Summary

The turbine aerodynamic performance is evaluated from BEM and CFD. The power curve prediction for both models appears in agreement. At high wind speeds stall regulation appear to happen. The thrust curve indicates a bad correlation of the models and this is attributed to the fact that the thrust model is purely theoretical for low axial induction factors, and also the fact that rotational effects are not accounted in the model. At high wind speeds, where typically high axial induction factors occur, the empirical BEM model is used where the analytical BEM thrust model breaksdown, and a good correlation is observed between the CFD and BEM model. The model Cp curve is evaluated for the sake of illustrating the wind turbine efficiency showing once again agreement of the models.

Stellenbosch University https://scholar.sun.ac.za

Part III

Coupler Electromagnetic Analysis

After the wind site assessment for the wind turbine suitability has been conducted and the cost impact of the wind turbine configuration has been determined, the electromechanical energy conversion system, specifically the slip permanent magnet coupler performance (slip-PMC) is evaluated taking into consideration the potential wind loading conditions evaluated and the wind turbine aerodynamic performance from Part II. The design operating speed of the slip-PMC is 150 rpm at a rated torque of $\pm$1000 Nm. This design point is chosen due the availability an existing prototype designed for the latter operating conditions in order to validate the slip-PMC concept and the models presented in this part of the thesis.

Stellenbosch University https://scholar.sun.ac.za

Chapter 8

Slip-PMC Models

8.1 Introduction

The slip permanent magnet coupler (slip-PMC) is typically used in transferring energy in a form of torque and power in rotary mechanical systems. One typical application of this machine is in wind energy systems where the mechanical torque induced on the wind turbine blades is transferred via the drive train to the slip coupler and finally to a synchronous generator feeding a stand-alone system or a grid. The slip-PMC is used as a means of regulating the induced torque on the drive train such that torque pulsations upstream on the turbine rotor side are damped through magnetic induction. In [44] the slip-PMC is introduced and in [21] different topologies of the slip-PMC are investigated, where in both papers the concept proved to be implementable for wind applications. What is of much interest from [21] is the non-overlap double layer coil configuration which has shown good performance for a machine of its type. Further in [23] a multiphase analysis technique is proposed for the FE analysis procedure, which proves to be accurate and computationally efficient. From the cited literature only surface mounted PM are proposed in the machine analysis. In this paper a spoke-mounted magnet configuration is proposed that concentrates the flux in the machine.

8.2 Slip-PMC Concept

The slip-PMC is a permanent magnet induction generator that converts high speed mechanical torque to low speed mechanical torque through the principle of magnetic induction. The device provides magnetic isolation between the high speed and low speed side of the drive train. This magnetic isolation provides a mechanical damping effect on the drive train where the step changes in high speed rotor side due to wind gusts are filtered and smoothed out at the low speed rotor end. The slip coupling operates at low slip frequencies where core losses are deemed negligible and the efficiency is thus assumed directly

Stellenbosch University https://scholar.sun.ac.za

proportional to slip ($\eta \approx (1 - s)$), where the only dominant losses considered in design optimisation are the copper losses in order to simplify the design optimisation process reducing the number of design variables.

8.3 Slip-PMC Configurations

The slip-PMCs are designed for high efficiency with minimum volume and mass. To reduce the cogging torque effect a high winding factor non-overlap winding machine is chosen [45, 46], since for wind energy applications at low wind speeds it is desired that the turbine starts easily. Various configurations are possible for the slip-PMC and only two configurations are evaluated in this study, namely:

1. surface-mount magnet type of rotor using magnets that are oriented radially and concentrating the flux radially as shown in Fig. 8.1.

2. spoke-mount magnet type of rotor using magnets that are oriented tangentially and concentrating the flux radially as shown in Fig. 8.2.

The advantage of the surface-mount PM machine is that the yoke lamination is a annular ring allowing ease of surface mounting the PM in manufacturing. The downside of surface mounted magnets is that the PMs are prone to fracture during construction and in operation which is detrimental to the health of the machine. Another downside is the radial attraction forces on the PM that may cause stress to the adhesive and eventually result in failure in the long run. An alternative PM rotor that can minimize the likelihood of PM fracture and machine health issues is sought to improve the reliability and robustness of the machine.

The spoke-mount magnet machine has a more elegant construction such that the attraction forces on the PM are oriented in the tangential direction. The construction of the PM rotor can be challenging, however, possible as a similar configuration is implemented in flux switching machines as discussed in Svetlik *et al* [47]. The shear stresses on the magnets and adhesive are reduced as the magnets would be embedded between steel blocks. In the event of accidental fracture the magnet fragments would be contained between the steel with the aid of adhesive and other containment measures. Spoke-mount magnet machines are reported to have a high power and torque density [24, 48].

The two machines shown in Figs. 8.1 and 8.2 comprise of short-circuited aluminum coils, permanent magnets and steel for the core. The coils are slotted over each tooth such that in a slot the coil sides are placed adjacent to each other.

Stellenbosch University https://scholar.sun.ac.za

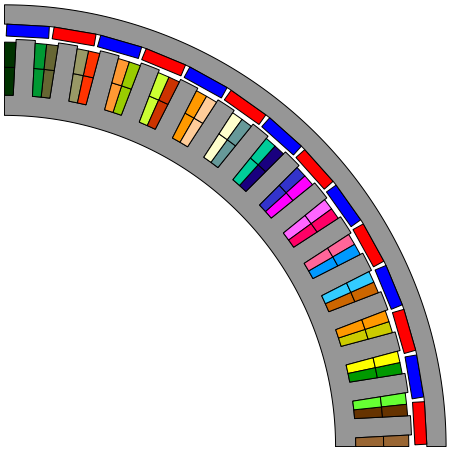

Figure 8.1: FE-model cross section of a 56-pole, 60-slot surface-mounted magnet slip-PMC [4].

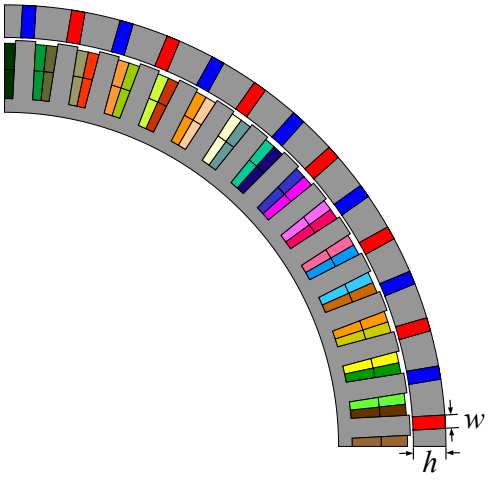

Figure 8.2: FE-model cross section of a 56-pole, 60-slot spoke-mounted magnet slip-PMC [4].

8.4 Slip-PMC Models

The two machine topologies' finite element (FE) analysis models are assumed to be the same. The induced rotor coil currents are assumed to be sinusoidal as was confirmed from the transient FEM simulation that was performed for both the spoke- and surface-mount PM machines in ANSYS Maxwell. With the assumed sinusoidal currents, the machines are modeled in the dq reference frame, with the dq-currents assuming dc values in static state.

Stellenbosch University https://scholar.sun.ac.za

8.4.1 dq Model for Non-Linear Analysis Technique

In steady state dq theory the flux linkages for coil layer i shown in Fig. 8.4 are given by

$$\lambda_{\mathrm{d}i} = L_{\mathrm{d}i} I_{\mathrm{d}i} + \lambda_{\mathrm{m}i}, \tag{8.4.1}$$

$$\lambda_{\mathrm{q}i} = L_{\mathrm{q}i} I_{\mathrm{q}i}. \tag{8.4.2}$$

The dq-voltage equations of the short circuited slip-PMC are derived directly from Fig. 8.3, which is the armature dq-circuit, with positive current taken as flowing into the machine. These dq-equations are given by (subscript $i = 1, ..., m$)

$$0 = R_i I_{\mathrm{d}i} - \omega_{\mathrm{sle}} L_{\mathrm{q}i} I_{\mathrm{q}i}, \tag{8.4.3}$$

$$0 = R_i I_{\mathrm{q}i} + \omega_{\mathrm{sle}} L_{\mathrm{d}i} I_{\mathrm{d}i} + \omega_{\mathrm{sle}} \lambda_{\mathrm{m}i}, \tag{8.4.4}$$

where R_i is the coil resistance, ω_{sle} is the operating electrical angular slip frequency, $I_{\mathrm{d}i}$ and $I_{\mathrm{q}i}$ are the dq currents. $L_{\mathrm{d}i}$ and $L_{\mathrm{q}i}$ are the dq inductances (including end-coil inductances) and $\lambda_{\mathrm{m}i}$ is the flux linkages due to the PMs. Using Eq. (8.4.1) - (8.4.4) and some mathematical manipulation we get

$$I_{\mathrm{d}i} = \frac{-\omega_{\mathrm{sle}}^2 L_{\mathrm{q}i} \lambda_{\mathrm{m}i}}{R_i^2 + \omega_{\mathrm{sle}}^2 L_{\mathrm{q}i} L_{\mathrm{d}i}}, \tag{8.4.5}$$

$$I_{\mathrm{q}i} = \frac{-\omega_{sle} R_i \lambda_{\mathrm{m}i}}{R_i^2 + \omega_{\mathrm{sle}}^2 L_{\mathrm{q}i} L_{\mathrm{d}i}}. \tag{8.4.6}$$

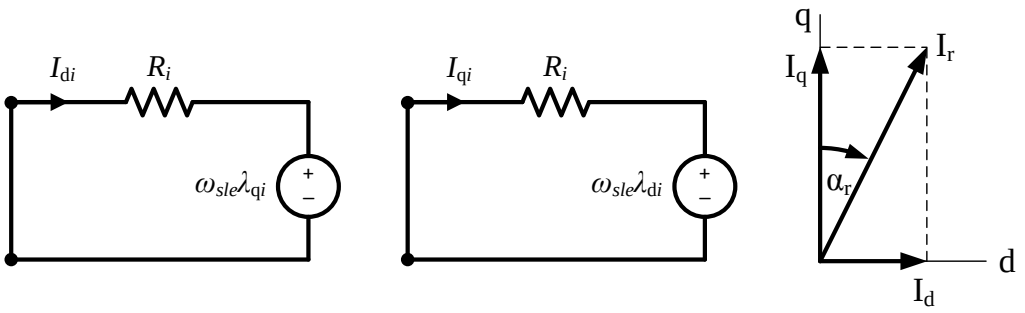

Figure 8.3: Steady state dq analytical circuit model [4].

8.4.2 *dq* Model for Linear Analysis Technique

The steady state dq flux linkages for coil layer i shown in Fig. 8.4 are given by:

$$\lambda_{\mathrm{d}i} = \sum_{j=1}^{m} M_{\mathrm{dd}ij} I_{\mathrm{d}j} + \sum_{j=1}^{m} M_{\mathrm{dq}ij} I_{\mathrm{q}j} + \lambda_{\mathrm{d_m}i} \tag{8.4.7}$$

Stellenbosch University https://scholar.sun.ac.za

$$\lambda_{\mathrm{q}i} = \sum_{j=1}^{m} M_{\mathrm{qq}ij} I_{\mathrm{q}j} + \sum_{j=1}^{m} M_{\mathrm{qd}ij} I_{\mathrm{d}j} + \lambda_{\mathrm{q_m}i} \tag{8.4.8}$$

where M denotes inductance which can be self- or mutual inductance, subscripts ij infer the flux linking circuit i to the current in circuit j with all other sources zero which is known as the mutual component, and ii is the self component, subscript dq or qd denotes the cross-coupling due to saturation effects. The self inductance, mutual inductance, self-cross coupling inductance, and mutual-cross coupling inductance are taken into account. This arguably completes the dq analytical circuit model, thus minimising uncertainties and due to the linear nature of the system of equations, improve convergence.
The speed voltages for coil layer i are given by: (subscript $i = 1, ..., m$)

$$0 = R_i I_{\mathrm{d}i} - \omega \lambda_{\mathrm{q}i} \tag{8.4.9}$$

$$0 = R_i I_{\mathrm{q}i} + \omega \lambda_{\mathrm{d}i} \tag{8.4.10}$$

After mathematically manipulating equations (8.4.7) - (8.4.8) we obtain the following coefficient matrices:

$$\mathbf{R}_i = \begin{bmatrix} R_i & 0 \\ 0 & R_i \end{bmatrix} \tag{8.4.11}$$

$$\mathbf{X}_i = \begin{bmatrix} \omega \sum_{j=1}^{m} M_{\mathrm{dd}ij} & \omega \sum_{j=1}^{m} M_{\mathrm{dq}ij} \\ -\omega \sum_{j=1}^{m} M_{\mathrm{qd}ij} & -\omega \sum_{j=1}^{m} M_{\mathrm{qq}ij} \end{bmatrix} \tag{8.4.12}$$

with

$$\mathbf{Z}_i = \mathbf{R}_i + \mathbf{X}_i. \tag{8.4.13}$$

The induced armature voltage and current matrix is respectively expressed by

$$\mathbf{V}_i = \begin{bmatrix} -\omega \lambda_{\mathrm{d_m}i} \\ \omega \lambda_{\mathrm{q_m}i} \end{bmatrix} \tag{8.4.14}$$

and

$$\mathbf{I}_i = \begin{bmatrix} I_{\mathrm{d}i} \\ I_{\mathrm{q}i} \end{bmatrix}. \tag{8.4.15}$$

The machine state equation is given by

$$\mathbf{I}_i = \mathbf{Z}_i^{-1} \mathbf{V}_i \tag{8.4.16}$$

The system of equations is then solved using numerical linear algebra. Fig. 8.4 illustrates the dq analytical model that is used in deriving the self, mutual and cross-coupling components of the analysis model.

Stellenbosch University https://scholar.sun.ac.za

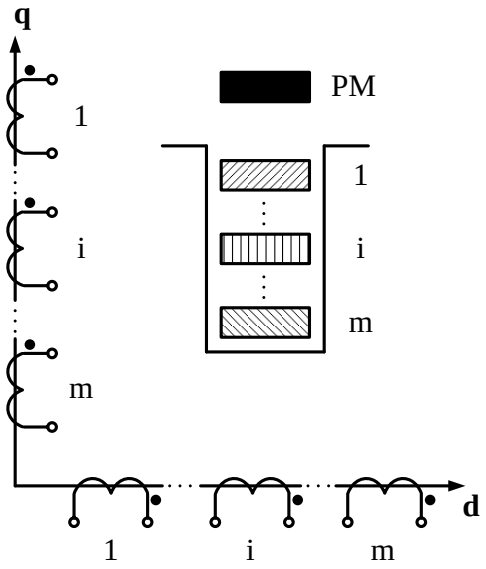

Figure 8.4: Model excitation layers for single layer PM, m coil layers. The *dq* analytical model self-, mutual- and cross-coupling components are derived with the aid of this diagram.

8.4.3 Torque Performance Model

The induced torque is determined by

$$T = \frac{N_s}{S} \sum_{i=1}^{2S/3} \frac{3}{2} \left(\frac{p}{2}\right) (\lambda_{\mathrm{d}i} I_{\mathrm{q}i} - \lambda_{\mathrm{q}i} I_{\mathrm{d}i}). \tag{8.4.17}$$

where S is the slots per machine section, hence $S = 15$ for the two machines of Figs. 8.1 and 8.2.

8.4.4 Conduction Loss Model

With the core losses assumed negligible due to low operating frequencies, the only losses considered in the design optimisation are the conduction losses which are determined as

$$P_{\mathrm{cu}} = T\omega_{\mathrm{sl}} = \frac{N_s}{S} \sum_{i=1}^{2S/3} \frac{3}{2} I_i^2 R_i, \tag{8.4.18}$$

where ω_{sl} is the mechanical angular slip velocity defined as

$$\omega_{\mathrm{sl}} = \omega_{\mathrm{R}} - \omega_{\mathrm{PM}}, \tag{8.4.19}$$

with ω_{R} as the coil rotor mechanical angular velocity and ω_{PM} is the PM rotor mechanical angular velocity. The electrical angular frequency is given by

$$\omega_{\mathrm{sle}} = \left(\frac{p}{2}\right) \omega_{\mathrm{sl}}, \tag{8.4.20}$$

Stellenbosch University https://scholar.sun.ac.za

where p is the number of poles. The system slip is defined as

$$s = \frac{\omega_{\text{sl}}}{\omega_{\text{PM}}}. \tag{8.4.21}$$

The phase peak current is given by

$$I_i = \sqrt{I_{\text{d}i}^2 + I_{\text{q}i}^2}. \tag{8.4.22}$$

The conduction loss obtained from both the static and dynamic FEM model is

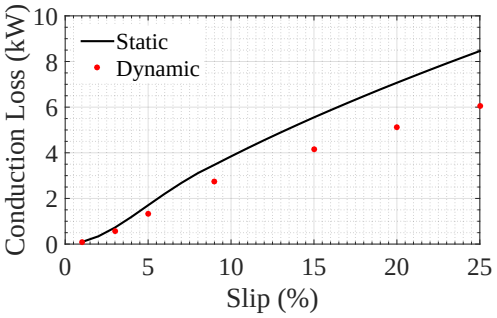

Figure 8.5: Conduction loss results in the static and dynamic FEM models for the spoke-mount PM machine.

presented in Fig. 8.5. At low slip values there appears to be agreement between the FEM models, however as the slip increases, the discrepancy appears to grow and this could be due to the solid loss solution given by the software which probably doesn't consider the end winding in the loss calculation. However the magnitude of the difference is large which doesn't seem to explain why it would be this large given the small end resistance which is expected to have a minor contribution to the conduction loss.

8.4.5 Core Loss Model

It is mentioned in section §8.4 that the core losses can be neglected in the design optimisation, but the question is how much is this core loss to be neglected and is it justified? In literature [49–51] various core loss models exist and in general they all considered to be dependent on the flux density (B_{max}), the magnetising frequency (f) and some proportionality constant (c). Generally the core loss consists of three components, namely hysteresis, eddy current and anomalous losses which is generally expressed as

$$p = p_{\text{h}} + p_{\text{e}} + p_{\text{a}}. \tag{8.4.23}$$

The core loss model proposed in [51] is chosen for convenience due to the availability of the model coefficients. This core loss model is expressed as

$$p = c_{\text{h}} f' B_{\text{max}}'^2 + c_{\text{e}} f'^2 B_{\text{max}}'^{(2+c_{\text{x}})} + c_{\text{a}} \left(f' B_{\text{max}}'\right)^{1.5} \tag{8.4.24}$$

Stellenbosch University https://scholar.sun.ac.za

where c_{h}, c_{e}, c_{a} denote the hysteresis, eddy and anomalous loss coefficients, and c_{x} is the exponent of the magnetic flux density. The scaled magnetic flux density and frequency are denoted by $B'_{\mathrm{m}} = B_{\mathrm{m}}/(1\mathrm{T})$ and $f' = f/(50\mathrm{Hz})$ where B_{m} and f are the maximum magnetic flux density and the operating frequency respectively. The maximum flux density is scanned for along the teeth of the wound rotor and f is the ac operating frequency. This model is implemented in conjunction with the static FEM analysis as a analytical tool in estimating the core losses in the slip-PMC, although the slip-PMC ac operating frequency range is low, it may be difficult to detect these losses accurately. However the results thereof will serve to justify the claim as to why the core losses may be neglected in future analytical analyses of such a machine operating at relatively low frequencies. The Ansys Maxwell dynamic FEM model, has a built in core loss model that is implemented as follows:

$$p_v = K_{\mathrm{h}} f B_{\mathrm{m}}^2 + K_{\mathrm{c}} \left(f B_{\mathrm{m}}\right)^2 + K_{\mathrm{e}} \left(f B_{\mathrm{m}}\right)^{1.5} \tag{8.4.25}$$

where K_{h}, K_{c}, K_{e}, denote the hysteresis, eddy and miscellaneous (excess) loss coefficients respectively. It is speculated that this expression might also be used in capturing the time harmonic components that might be significant in the loss calculation. Any discrepancy between the static and the dynamic core loss calculation may be attributed the static FEM model considering only the fundamental frequency and the dynamic FEM model considering the whole frequency spectrum (harmonics). The core loss from the static and dynamic model, shown in Fig. 8.6, indicates a strong correlation, with marginal discrepancies, as the dynamic model core loss results exhibit some slight scattering. At rated slip conditions which is 3%, the conduction loss to core loss ratio is 10, indicating factor ten difference. Further at higher frequencies, the ratio increases to 13.33-18.89 indicating a growth in the negligibility of the core loss grows with increase in slip values.

Table 8.1: Steinmetz coefficients used in the static core loss calculation

coefficient	c_{h}	c_{e}	c_{a}	c_{x}
value	0.3526	0.1780	0.4831	1.1990

Table 8.2: Steinmetz coefficients used in the dynamic core loss calculation

coefficient	K_{h}	K_{c}	K_{e}
value	17.63	445	170.80

Stellenbosch University https://scholar.sun.ac.za

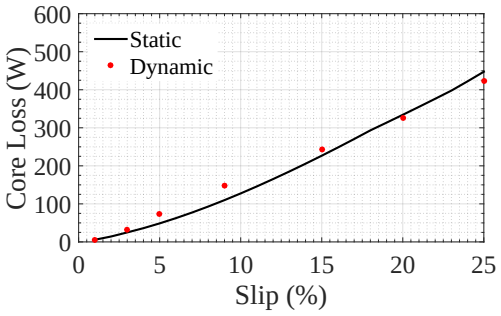

Figure 8.6: Core loss results from the static and dynamic FEM model for the spoke-mount PM machine.

8.5 Summary

The slip-PMC regulates torque pulsations upstream, damping them through magnet induction. Two topologies of the slip-PMC are introduced, namely surface- and spoke-mount PM machines. The analysis of slip-PMCs is introduced for a linear and non-linear analysis. Where the linear model is deemed to capture cross-coupling, mutual coupling, which are neglected by the non-linear model. The linear model shows better convergence rate, however, the additional solver used to solve the linear equations comes at an additional cost of CPU time, however giving more accurate results, especially where saturation effects are dominant. The conduction and core losses in the machine are presented. The core loss assumption, that states that the core losses in the slip-PMC is negligible is justified in this chapter, using the static and dynamic FEM models for the core loss calculation. The core loss models implementation may be different however the results illustrate good agreement.

Stellenbosch University https://scholar.sun.ac.za

Chapter 9

FE Analysis Techniques

9.1 Introduction

The slip-PMCs shown in Figs. 8.1 and 8.2 are modeled and simulated in a in-house 2-D static finite element method (FEM) package called SEMFEM and in a commercial transient state FEM package called ANSYS Maxwell. As seen in both Figs. 8.1 and 8.2 each coil is partitioned into multiple layers for the sake of 2D static analysis in order to capture the slot leakage effect [50] as the FEM solver demonstrated improved results, especially at higher operating frequencies. The analysis procedure followed in the design performance evaluation is presented in this chapter.

9.2 Non-Linear Permeability Analysis Procedure

The details of the analysis technique used in this thesis are discussed in Van-Wyk [23]. However in this manuscript the analysis technique is illustrated as shown in Fig. 9.1. This analysis technique is used for determining the induced current in the machine coil through the principle of induction. The induced current is first guessed from the rated copper loss which is calculated from Eq. (8.4.18) knowing the initial estimate of the rated torque and rated slip speed of the coupler. For the initial guess the copper loss current is assumed to be the q-axis current and zero current is assumed for the d-axis current to satisfy the condition $\lambda_{\mathrm{m}} = \lambda_{\mathrm{d}}$. The FEM solver is driven with this initial estimation current as input current. In post-processing the dq flux data from the FEA solver, the dq inductances are determined using Eq. (8.4.1) and (8.4.2) and the previous current solution. Then the resultant dq current is evaluated using Eq. (8.4.5) and (8.4.6). The resultant current is evaluated against the previous current, and if the solution error exceeds the maximum error threshold e_{max} the resultant current is used as the input current and the process is repeated

Stellenbosch University https://scholar.sun.ac.za

as shown in Fig. 9.1 until convergence is reached. The copper loss is denoted by P_{cu}, R represents the coil resistance, n is the iteration step, ω_{sl} is the slip angular speed, λ_m denotes the flux linkage due to the magnet, e and e_{max} are the solution error and the user specified maximum convergence error respectively. The solution output $[\mathbf{Y}]$ is the user specified performance parameters vector. This process is implemented for static conditions.

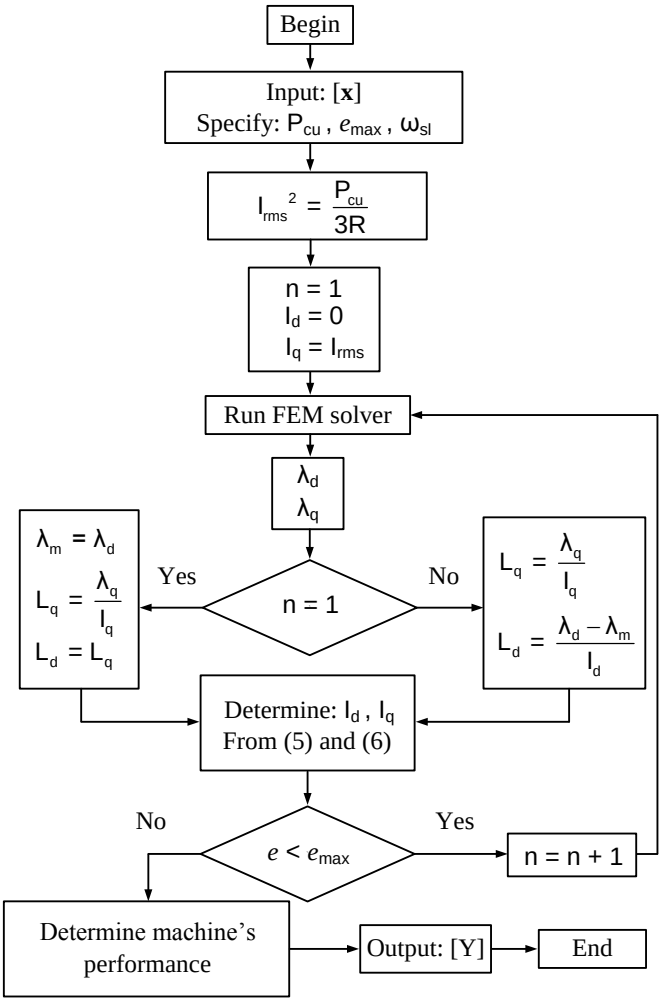

Figure 9.1: Analysis method flow chart for solving currents and induced torque of the slip-PMC [4].

9.3 Linear Permeability Analysis Procedure

In the linear permeability analysis method, first a non-linear solution is sought using the initial inputs. The resulting permeabilities from the non-linear solution are stored for each mesh element. Then a linear solution is run where the

Stellenbosch University https://scholar.sun.ac.za

flux linkage due to the field magnets on the coils is first captured as $\lambda_{\mathrm{d_m}i}$ and $\lambda_{\mathrm{q_m}i}$ under no load. Subsequently the field magnets are unexcited where only the current excitation for each coil layer is applied, whether it be d- or q-axis current and the corresponding flux linkage $\lambda_{\mathrm{d}i}$ and $\lambda_{\mathrm{q}i}$ is captured and their corresponding inductances $M_{\mathrm{dd}ij}$, $M_{\mathrm{dq}ij}$, $M_{\mathrm{qq}ij}$ and $M_{\mathrm{qd}ij}$ are determined using the flux linkage expressions given by Eq. (8.4.7) and (8.4.8). Once the self, mutual and cross-coupling inductances have been determined, the impedance coefficient matrix $\mathbf{Z}_i$ is created using the resistance and reactance matrix given by Eq. (8.4.11) and (8.4.12). The impedance coefficient matrix is inverted then the armature voltage coefficient matrix Eq. 8.4.14 is setup using Eq. (8.4.14) thus the induced eddy current solution 8.4.16 is obtained iteratively in this fashion.

9.4 Convergence Criterion

The solution parameters that are monitored for convergence are the induced eddy current solution for each coil layer individually. The convergence criteria is set as such

$$|x_{\mathrm{new}} - x_{\mathrm{old}}| \leq \epsilon * \left| \frac{x_{\mathrm{new}} + x_{\mathrm{old}}}{2} \right| \tag{9.4.1}$$

where ϵ is the specified solution tolerance, x_{new} and x_{old} are new and old solver solutions. The convergence parameters monitored are the induced eddy currents $d-$ and $q-$axis components, monitored individually for each coil layer. And the solution is deemed converged once all the dq-current components have converged to within the allowable solution tolerance level.

9.5 Analysis Technique Performance Results

After the implementation of the linear and non-linear analysis technique, the torque versus slip performance illustrated in Fig. 9.2 is obtained. Both method are in good agreement in the $0-9\%$ slip range, which is considered the linear region where saturation effects in the machine core are negligible. In the slip range greater than 9%, a discrepancy arises from the analysis methods which can be attributed to the cross-coupling and mutual inductance components that are neglected by the non-linear method. This analysis is run assuming only the dc resistance characteristic. Running a performance comparison of the two analysis methods serves to verify the methods and to demonstrate how the assumptions made in the methods affect the solution accuracy.

Stellenbosch University https://scholar.sun.ac.za

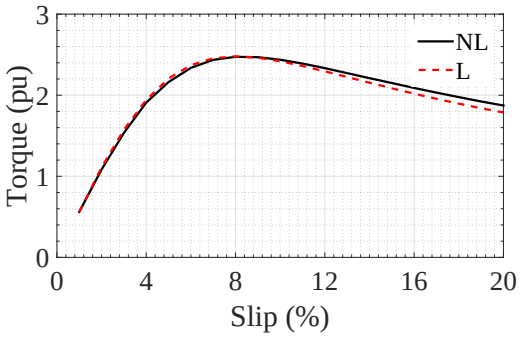

Figure 9.2: The torque performance of the spoke-mount PM slip-PMC using the linear and non-linear technique for analysing the machine performance.

9.6 Convergence Rate of Analysis Methods

The convergence rate of the analysis methods is evaluated in this section in order to establish the stability of the solver. In Fig. 9.3 is the convergence rate of the analytical solvers assuming only the dc resistance in the coils. The non-linear analysis method in general exhibits a slow convergence rate when compared to the linear analysis method especially when a convergence criterion is set in the solver as discussed in §9.4. The non-linear model analysis method, given its simplicity, performs well especially in the linear operating region as shown in Fig. 9.3a. However as the machine gets more loaded, the core gets more saturated, and the number of iterations required increases. In the linear model case fewer iterations are required due to the linear nature of the FEM model and the analytical model, whereas the non-linear case requires more iterations to converge. When the multiple layer model is considered the solver convergence rate is as shown in Fig. 9.3a, exhibiting similar behaviour as that of Fig. 9.3b. However the only observed effect was on CPU time, as the more equations there are to solve the more computation time is required to obtain a solution. An attempt to save on computation time by reducing the number of coil layer i.e. number of equations comes at a cost of solution accuracy as will be illustrated in Chapter 10.

Stellenbosch University https://scholar.sun.ac.za

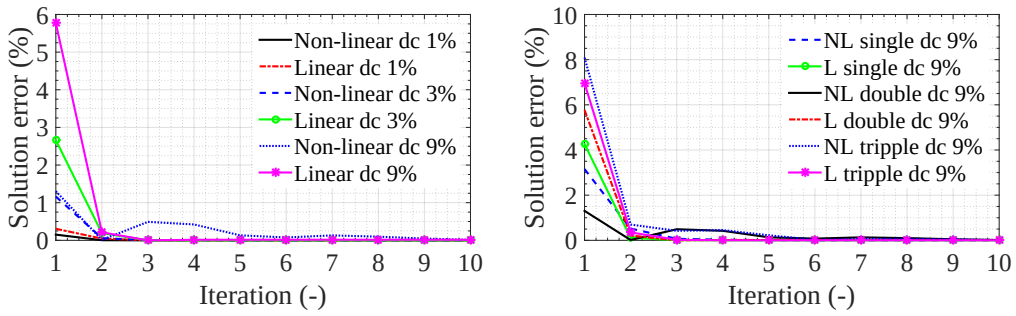

(a) (b)

Figure 9.3: The convergence rate study of the linear and non-linear analysis techniques with (a) demonstrating the slip range convergence rate with dc resistance and (b) demonstrating the coil layer model convergence rate.

9.7 Summary

The FE analysis techniques and procedures for the linear and the non-liner FE models are presented. The convergence criterion used in monitoring convergence is presented, where the induced currents are chosen as convergence parameters. Generally both models exhibit good convergence rates when the machine loads are considered below core saturation. However under high frequency high loads/saturation the convergence rate of the non-linear model becomes slower.

Stellenbosch University https://scholar.sun.ac.za

Chapter 10

Conductor Impedance

10.1 Introduction

The conductor in the static FEM analysis requires special treatment in order to capture the slot leakage effect and the skin effect. A dc-ac resistance technique is employed in attempt to improve accuracy and correlate the static FEM model to the time harmonic FEM model. Another challenge is the slot leakage effect that is due to the flux produced by the field magnets not linking with the coils. Presented in this chapter are the coil resistance models, the slot leakage technique, the coil end effects and the temperature effect consideration on the coils resistivity.

10.2 Skin Effect

The skin effect in the proposed machines coil layout is due to the induced eddy currents in the coils that tends to shield the bottom section of the coils as illustrated in Fig. 10.1b. The theory of penetration of electromagnetic fields into a conductor assumes that the coil is of infinite depth and that there is no field variation along the width or axial length of the conduction medium. The internal impedance of the conductor is computed in the same manner as that of a plane conductor. The decay of the of the fields into the conductor are viewed as the attenuation of a plane wave as it propagates into the conductor or from the point of view that induced fields from time varying currents tend to counter the applied fields [52]. The non-uniform current distribution that is caused by the skin effect, results in an increase in the effective coil impedance, thus influencing the machine performance.

10.2.1 Coil Resistance Model

Under low frequency conditions, the coil resistance is assumed constant with the field frequency, as the coil shielding effect may be assumed negligible. The

Stellenbosch University https://scholar.sun.ac.za

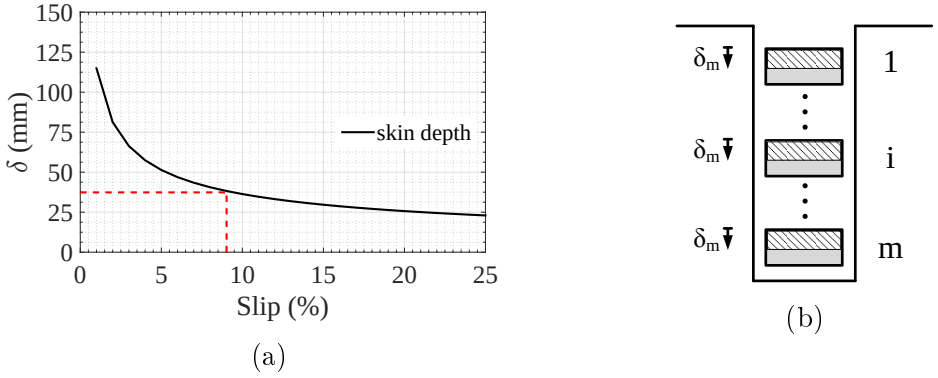

Figure 10.1: A simple skin depth illustration where (a) is the skin depth plot as a function of slip and (b) is the skin depth of penetration of skin effect distribution on coil layers.

dc resistance of the conducting medium is described by:

$$R_{\mathrm{dc}} = \frac{l}{\sigma A} \tag{10.2.1}$$

where σ is the material conductivity, l is the conductor length and A is the conductor cross-sectional area perpendicular to the current flow path. At high field operating frequencies the coil shielding effect becomes prominent where the skin effect affects the machine performance. The skin resistance is given by

$$R_s = \frac{1}{\sigma\delta} = \sqrt{\frac{\pi f \mu}{\sigma}} \tag{10.2.2}$$

where σ is the material conductivity, f is the operating field frequency, μ is the conducting medium permeability, and δ is the field depth of penetration. The field depth of penetration is characteristic of the conductive material and the field operating frequency.

The ac resistance is then determined as follows

$$R_{\mathrm{ac}} = R_{\mathrm{s}} \frac{l}{w} \tag{10.2.3}$$

where R_{s} is the skin resistance, l is the conductor length, and w is the conductor width. The skin depth of penetration distribution in the coil layer is given by

$$\delta_{\mathrm{m}} = \frac{\delta}{\mathrm{m}} \tag{10.2.4}$$

where δ is the overall skin depth on the coil side and m is the number coil model layers, as shown in Fig. 10.1b. The skin depth versus slip is shown in Fig. 10.1a and the skin depth is approximately 38 mm at slip of 9%. This skin depth is approximately equal to the coil's physical depth. This slip value is where the ac resistance picks up, dominating over the dc resistance.

Stellenbosch University https://scholar.sun.ac.za

10.2.2 Slot Leakage Model

The multi-layer coil modelling enables the accurate capture of the slot leakage effect which occurs mostly at the lower section of the coil. The dq model indicates this and the machine torque prediction shows this effect at play in both low and high slip values. Effectively the accuracy of the machine performance prediction is improved by this modelling strategy. The slot leakage is captured in terms of the machine inductances that result from the analysis method. The non-uniform current distribution in the coils is approximated through this slot leakage modelling technique. Fig. 10.2 illustrates the slot leakage that occurs at the bottom of the slot and top of the slot with some cross flux that contributes to the impedance of the coils.

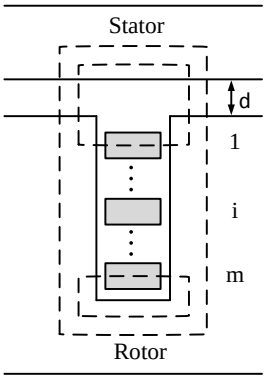

Figure 10.2: Slot leakage effect model in static FEM.

10.3 End Winding Effects

The end effects considered here are those due to the coil ends protruding from the wound rotor's axial stack length.

10.3.1 End Winding Resistance

The end resistance is calculated by using the normal dc resistance formula,

$$R_e = \rho \frac{l_e}{A} \tag{10.3.1}$$

where ρ is the conductor resistivity, A is the conductor's effective cross-section area, and l_e is the end winding length. In this case, it is assumed that the end winding resistance is constant in the simulation models. However, the ac resistance model can be employed in the end winding resistance calculation.

Stellenbosch University https://scholar.sun.ac.za

10.3.2 End Winding Inductance

In Honsinger [53], the analytical end winding inductance models, for end windings of various shapes, are derived. The end winding inductance derivation procedure assumes line currents in the end winding coils and then further uses the energy equation that states that the energy stored in a inductor is directly proportional to the square of the current in the inductor and its inductance. That it is how the derivation of the end wind inductance proceeds to yield the end winding inductance models presented in his paper. The end wind inductance model is given by

$$L_e = 1.8 m_e \left(\frac{C k_{dp}}{p} \right)^2 k_s^2 k_e k_m \times 10^{-8} \tag{10.3.2}$$

where k_s is the coil shape factor for individual coil, k_e is the end winding factor, p is the number of poles, C is the number of conductor in series per phase, m is the number of phases, k_{dp} is a product of the ordinary distribution factor k_d and the end winding pitch factor k_p, k_m is the mutual inductance factor, and e is the end winding radius for the rotor. This model is considered to apply to squirrel-cage and wound rotor machines [53]. The value is a static value, which indicates that the skin effect is not considered in the end winding model formulation.

10.4 Resistivity Temperature Effects

As the machine operates for long periods of time the coil temperature increases above ambient temperature and thus the resistivity of the conductor increases in direct proportion to temperature as the conductor resists the flow of current. In effect the coil resistance is affected by temperature variations, in turn affecting the machine performance. It is important to account for the temperature effect to especially model the coils resistance at a given temperature. The temperature effect on resistivity is represented by

$$\rho_{\text{new}} = \rho_{\text{ref}} \left[1 + \alpha_{\text{t}} \left(T - T_{\text{ref}} \right) \right], \tag{10.4.1}$$

where ρ_{ref} is the reference resistivity at ambient temperature typically 20°C, α_{t} is the temperature coefficient that is characteristic of the conducting material, T_{ref} is the reference temperature, T is the coil temperature and ρ_{new} is the new resistivity of the conducting material at the coil temperature.

10.4.1 Coil Resistance Calculation Procedure

The machine coils are 38 mm in depth, thus using the skin depth graph one can be able to determine when the skin effect will be dominant by determining the conductor's internal impedance. The procedure to calculate the internal

Stellenbosch University https://scholar.sun.ac.za

resistance of the conductor uses both dc resistance and ac resistance. There is a criteria set to determine when the resistance is to be determined as either dc or varying with frequency. By using Eq. (10.2.1) and (10.2.3) the following criteria is used in evaluated the coil resistance with operating frequencies:

- if $R_{\text{dc}} > R_{\text{ac}}$ then the effective resistance set to the dc resistance value i.e. $R_{\text{eff}} = R_{\text{dc}}$
- else if $R_{\text{dc}} < R_{\text{ac}}$ then the effective resistance takes on the values of the ac resistance i.e. $R_{\text{eff}} = R_{\text{ac}}$.

The ac resistance improves the performance prediction and allows the method to be more stable especially at high frequencies. A damping effect is introduced by the ac resistance at hight frequencies to allow the performance prediction especially the torque prediction to be more stable and sensible, especially that of torque. The damping effect also improves the solution convergence rate.

10.5 Results

Shown in Fig. 10.3 is the slip-PMC torque performance considering the dc resistance and ac resistance effect on the torque performance prediction, particularly at high slip values. The slot leakage effect is also accounted for by modelling multiple layers of the coil sides in the FEM model. The effect of the slot leakage is demonstrated in the results of Fig. 10.3a where with an increase in the coil model layers, the torque prediction converges to some final value at high slip values. It was noted in §9.6 that the convergence rate of the model with dc resistance under high loading condition tends to be slow. With the ac resistance, the convergence rate of the model improved becoming fast. The ac resistance effect at high frequencies is demonstrated by Fig. 10.3b, this performance prediction is important for motor application where typically at start-up the wound rotor field frequency may be high. Thus a more accurate prediction of the starting torque may be achieved as shown in Fig. 10.3.

10.6 Summary

The skin effect greatly influences the slip-PMC performance, thus a model to account for this effect is presented. The slot leakage model by means of multiple coil layer modelling shows improved performance prediction accuracy. The end winding effects and temperature on the coils is considered. The dc-to-ac and vice versa criterion is determined, where it is found that the ac resistance is dominant whenever the skin depth of penetration is less than the coil physical depth in to the slot. The performance prediction improvement is demonstrated by the slot leakage effect, which shows improvement for up to 3 coil layers.

Stellenbosch University https://scholar.sun.ac.za

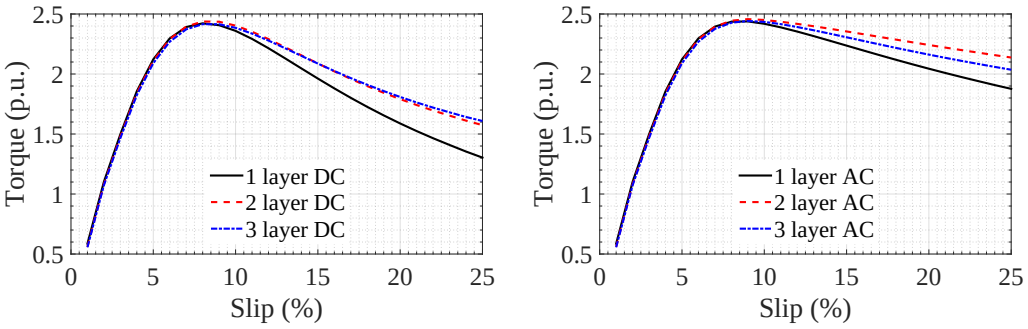

(a) (b)

Figure 10.3: The skin effect with (a) demonstrating the slot leakage effect with dc resistance and (b) the skin resistance effect with dc resistance at low frequencies and ac resistance at high frequencies

.

Stellenbosch University https://scholar.sun.ac.za

Chapter 11

Magnetic Properties

11.1 Introduction

The permanent magnets which have produced the largest magnetic flux with the smallest mass are the samarium and neodymium based rare earth magnets. Their high magnetic fields and light weight make them attractive. However the extensive use of rare earth magnets demands that less of this material be used and the reliability of it in electric machines be improved.

11.2 B-H Characteristic

A simple linear B-H characteristic is assumed for the PM. Demagnetization effects are not considered since the machine is singly excited by the PM only, thus the induced currents in the machine are assumed to be such that they do not demagnetize the PM. The B-H characteristic is represented by

$$\mathrm{B_r} = \mu_\mathrm{r}\mu_0\mathrm{H_c} \tag{11.2.1}$$

where $\mathrm{B_r}$ is the remnant magnetic flux density, μ_r is the relative permeability of the magnet material, μ_0 is the permeability of free space and $\mathrm{H_c}$ is the magnet coercivity. The permanent magnet coercivity is the amount of applied or external magnetic field required to demagnetise the permanent magnet. Fig. 11.1 shows the FEM model of the M530-65A steel bh-curve and the neodymium-iron-boron permanent magnet which is a rare earth permanent magnet with a remnant magnetic field density of 1.34 T and a relative permeability of $\mu_r = 1.05$.

11.3 PM End Effects

The PM end effects considered here are the fringing flux that occurs on the magnets. This leakage flux greatly impacts the performance of the electrical

Stellenbosch University https://scholar.sun.ac.za

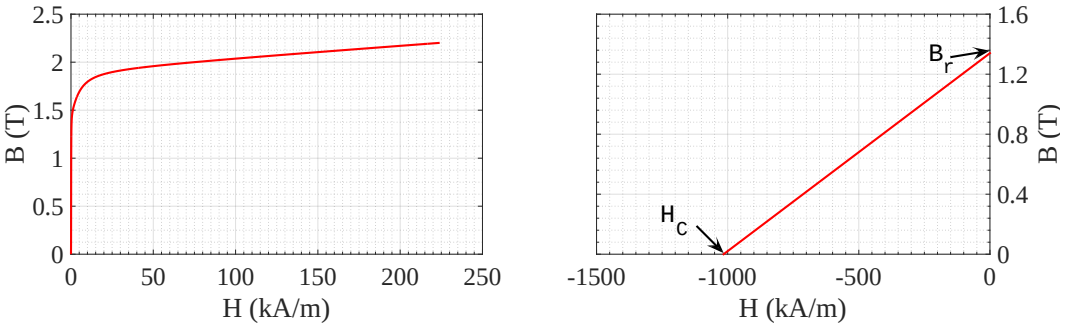

(a) (b)

Figure 11.1: The bh characteristic of the (a) M530 65A steel, and (b) NdFeB magne.

(a) (b)

Figure 11.2: The leakage flux interaction in the machine where (a) is the inter-pole flux leakage, and (b) is the pole self flux leakage.

machine by reducing the effectiveness of the permanent magnets depending on the magnet configuration. In the case of the spoke-mount permanent magnet machine shown in Fig. 11.2b, the PM flux leakage appears sensitive to the zero potential boundary indicating that a tremendous leakage flux occurs there. The surface-mount permanent magnet configuration shown in Fig. 11.2a confines the flux to within the machine volume. On the surface-mount permanent magnet machine there is some free flux that occurs outside the machine. To illustrate the influence of the field magnet orientation on the flux linkage which greatly determines the armature back emf, the no load flux linkage of the surface-mount and spoke mount PM configuration are analysed. The flux linkage are obtained for the same amount of permanent magnet material in both machines from the static and dynamic FEM models. Given in Table 11.1 are the *dq* flux linkage obtained from the FEM models, noting that there is an agreement in the results with a deviation of the d-axis flux linkage 4% in error from the static FEM model. The error can be attributed to the time harmonics, as a single step static FEM solution is used in the results. The spoke-mount permanent magnet flux linkage on the armature is given in Table 11.2 with the static d-axis flux linkage deviating by 1% from the dynamic flux linkage. Clearly in Table 11.1 and 11.2 one observes the large discrepancy on the flux linkages induced in the coils. The discrepancy is 28.84% from the surface mount permanent magnet machine. Which could explain the differ-

Stellenbosch University https://scholar.sun.ac.za

ence in the break down torque of the two machine topologies. Illustrated in Fig. 11.2a and 11.2b is the leakage flux between the magnet poles due to their close proximity to each other. The author terms this the inter-pole leakage flux. Another observation is that the d axis flux linkages from the both the static and dynamic FEM are not the same, which is largely responsible for the induced torque in the machine in generator mode. High dq flux linkages are generated for the spoke-mount PM machine when compared to those of the surface-mount PM machine. This serves to illustrate the discrepancy in the solution currents and torque obtained in the static and dynamic FEM models.

Table 11.1: No load flux linkages induced in the surface-mount PM machine

	Maxwell Ansys (dynamic)	SEMFEM (static)
λ_d (mWb·turns)	0.9402	0.9500
λ_q (mWb·turns)	0.0166	0.0000

Table 11.2: No load flux linkages induced in the spoke-mount PM machine

	Maxwell Ansys (dynamic)	SEMFEM (static)
λ_d (mWb·turns)	1.1776	1.1224
λ_q (mWb·turns)	0.0165	0.0005

11.4 Summary

The bh curves of the M530-65A steel and the NdFeB PM magnet are presented. The demagnetisation effect on the PM are neglected. The leakage flux on the PM rotor are highlighted for both the surface- and spoke-mount PM machine model. The no load flux linkage for each model are presented from both a static and dynamic model perspective. For the same amount of PM material, the spoke-mount PM machine shows a high flux linkage, which results in higher induced armature voltage and thus currents. This explains the discrepancies in the two machine model performance predictions.

Stellenbosch University https://scholar.sun.ac.za

Chapter 12

FEM Model

12.1 Introduction

The FEM model boundary conditions assignment, governing equations used in FEM and the interfacing of the FEM model with the analytical model are introduced in this chapter. This is done to give a clearer picture of how the FEM model and the analytical model communicate with each other. Also highlighted are the loop holes in the analytical model assumptions used in the static simulation.

12.2 Boundary Conditions

The electric machine model is quarter symmetric, which allows only one-fourth of the machine to be modeled in FEM. The periodicity is even symmetric due to the even numbered poles and the currents in the machine phases are periodic every 90° mechanical (spatial) angle. A Dirichlet boundary is set on the free space far field region to zero potential shown in Fig. 12.1. A Neumann condition is prescribed on the periodic boundaries, stating that the flux gradient is zero $\frac{\partial \phi}{\partial \mathrm{n}} = 0$ on the boundary. On one of the models the PM rotor yoke imposes a shielding effect such that the flux is confined within the machine volume. The spoke-mount PM machine model has free flux on the PM rotor, thus not confining the flux to the volume of the machine, however, the FEM appears to be sensitive to where the shielding boundary is placed relative to the machine boundary.

How large a portion of the machine needs to be modelled in order to have a balance between the number of poles and number of slots [54] can be determined by using

$$F = \gcd\left(N_{\mathrm{s}}, N_{\mathrm{m}}/2\right) \tag{12.2.1}$$

where F is the greatest common divisor of number of slots (N_{s}) and the number of poles ($N_{\mathrm{m}}/2$). The value obtained from Eq. 12.2.1 is indicative of the

Stellenbosch University https://scholar.sun.ac.za

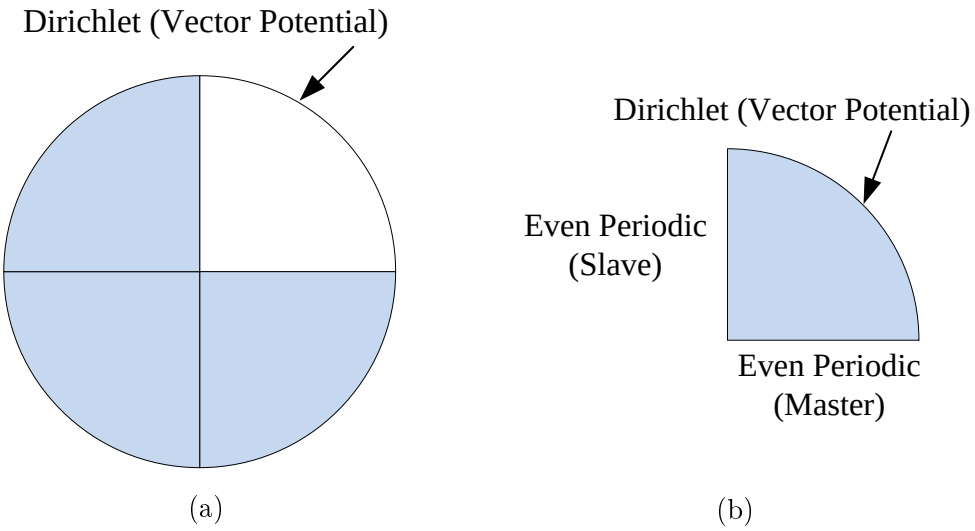

Figure 12.1: Model boundary condition and the advantage of symmetry.

fraction of the machine sufficient in the FEM model. In the case of the machine models presented in this thesis, a value of $F = 4$ is obtained thus implying that only 1/4th of the machine can be modelled, which results in reduced simulation time in both the static and the dynamic model. The interaction

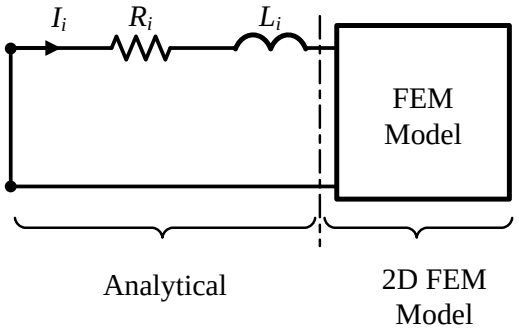

Figure 12.2: Finite element and analytical model interaction.

of the FEM model and the analytical model is illustrated by Fig. 12.2 for a singly PM excited machine. The interfacing is such that the FEM model solves the EM fields and outputs the flux linkages which are used as source in the analytical model to establish the induced armature voltage and currents.

12.3 Dynamic and Static FE Model

In this section the governing equations of the time harmonic and static FEM models are introduced. It is important to examine them in order to compre-

Stellenbosch University https://scholar.sun.ac.za

hend how the induced eddy currents are determined. Coupled to these models are the analytical circuit models that model the impedance of the ends in the case of the transient model and the whole conductor in the case of the dynamic model. To begin let's look at the field magnetisation characterisation due to a PM which is given by

$$\boldsymbol{B} = \nabla \times \boldsymbol{A} = \mu \boldsymbol{H} + \boldsymbol{M} \tag{12.3.1}$$

where $\boldsymbol{A}$ is the flux vector potential, μ is the magnetic material permeability, $\boldsymbol{H}$ is the applied field intensity, $\boldsymbol{M}$ is the magnetisation due to the permanent magnets.

12.3.1 Dynamic Governing Equations

In the time harmonic model, the vector potential formulation assumes eddy and source currents expressed by

$$\nabla \times \left(\frac{1}{\mu}\nabla \times \boldsymbol{A}\right) = \sigma\left(-\frac{\partial}{\partial t}\boldsymbol{A} - \nabla\phi\right) + \frac{1}{\mu}\nabla \times \boldsymbol{M} \tag{12.3.2}$$

where the term on the right hand side of the equation represents the conduction current density, which is also known as the eddy current expressed as follows:

$$\boldsymbol{J} = \sigma \boldsymbol{E} = \sigma\left(-\frac{\partial}{\partial t}\boldsymbol{A} - \nabla\phi\right) \tag{12.3.3}$$

where $\boldsymbol{E}$ represents the electric field density, $\nabla\phi$ is the electric potential due to the spatial curvature or spatial variation of the electric potential in the magnetic field, $\frac{\partial}{\partial t}\boldsymbol{A}$ is the time variation of the vector potential. Additionally, when linearity is assumed the current density may be assumed as follows

$$\boldsymbol{J} = \sigma\left(-j\omega\boldsymbol{A} - \nabla\phi\right) \tag{12.3.4}$$

where ω is the field operating frequency, with j indicating that the quantity is sinusoidal.

12.3.2 Static Governing Equations

The static model assumes the following vector potential formulation,

$$\frac{1}{\mu}\nabla \times \nabla \times \boldsymbol{A} = \boldsymbol{J} + \frac{1}{\mu}\nabla \times \boldsymbol{M} \tag{12.3.5}$$

where $\boldsymbol{J}$ is the prescribed source current density, and the second term on the right hand side of the equation is the equivalent magnetic current density.

Stellenbosch University https://scholar.sun.ac.za

In the analytical induced eddy current formulation, it appears that the model assumes linear properties and neglects the spatial variation of the flux i.e. assumes the $\nabla\phi$ term of the eddy current formulation to be zero. The current density $\boldsymbol{J}$ is prescribed in Eq. 12.3.5 is determined by using the models and methods discussed in Chapter 8 and 9.

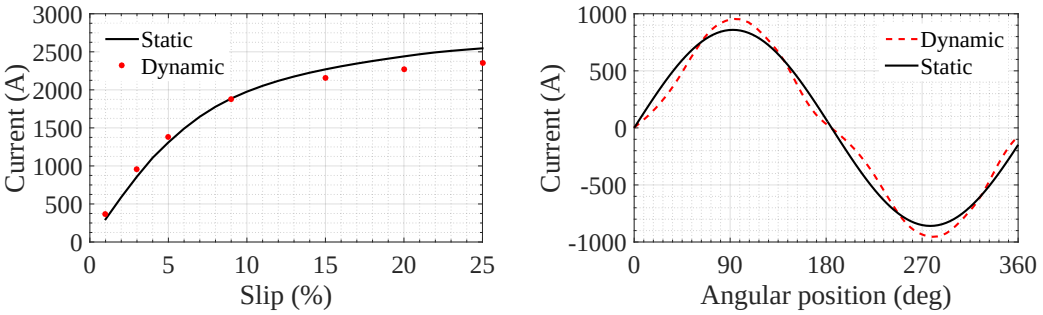

(a) (b)

Figure 12.3: Induced current (a) peak current magnitude and (b) the current waveforms obtained from the spoke-mount PM machine.

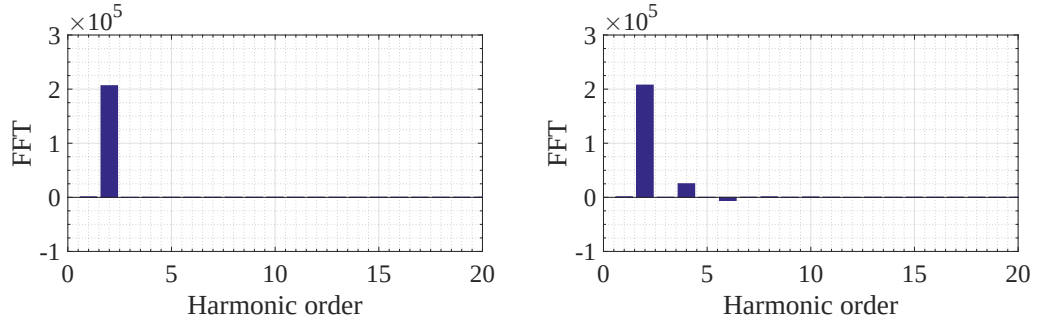

(a) (b)

Figure 12.4: Induced current harmonics from the (a) static and (b) transient FEM model for the spoke-mount PM machine.

The discrepancies observed in the machine performance prediction obtained from the static and dynamic model can be justified by the time harmonic components of the electrical fields. For example shown in Fig. 12.4a are the induced current time harmonics assumed in the static FEM model and in Fig. 12.4b are the time harmonics that emerge from the time harmonic FEM solution. There seems to be prominent 3rd and 5th harmonic components that arise from the time harmonic FEM solution, and this could be the result of

Stellenbosch University https://scholar.sun.ac.za

the discrepancy in the induced current magnitude and induced torque that has been highlighted in earlier sections/chapters.

12.4 Results

The induced currents from the static and dynamic FEM model are shown in Fig. 12.3. When a slip frequency sweep is performed the induced peak current value shown in Fig. 12.3a are obtained. The induced currents from the FEM models are in agreement with some discrepancies that are assumed to be due to the model formulation assumptions. Fig. 12.3b illustrates the harmonic distortion that is observed in the time harmonic induced current plot and how that is different to the static induced current, that is assumed purely sinusoidal. Also observed are the discrepancies in the peak induced current. The highlighted discrepancies are assumed to be responsible for the discrepancies observed in the torque performance predictions as will be demonstrated in Chapter 13.

12.5 Summary

The core FEM governing equations for the static and dynamic model are presented in order to better understand, appreciate and highlight assumption made by each model and the reasons as to why one would observe discrepancies in results obtained from the FEM model predictions. It is shown that in the static FEM model, the induced currents are specified as source currents, which are determined using the analytical models of Chapter 8 and the analysis techniques of Chapter 9. In the dynamic FEM the induced currents are determined by the non linear time variation of the flux and spatial variation of the flux, resulting in the induced armature voltage and currents. The harmonics on the assumed induced current in static model and resulting dynamic induced currents from the dynamic model are highlighted with differences in shape and amplitude of the current waveform.

Stellenbosch University https://scholar.sun.ac.za

Chapter 13

Design Optimization

13.1 Introduction

The slip-PMC's outer PM rotor is optimized for the fixed inner wound rotor size on the preexisting prototype shown in Fig. 13.9a. The optimization is performed for the spoke-mounted PM rotor configuration in Fig. 8.2. One would like to see how the variation in magnet width and height affects the PM mass, active mass and performance of the machine.

The dimensional parameters that have to be optimized in the design are

$$[\mathbf{x}] = \begin{bmatrix} h \\ w \end{bmatrix}, \tag{13.1.1}$$

where h is the magnet height and w is the magnet width as indicated in Fig. 13.1.

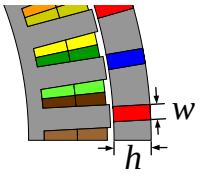

Figure 13.1: Optimisation dimensions.

13.2 Optimization Maximizing Torque

In the first optimization the objective function $F(\mathbf{x})$ to be maximized is the torque of the coupler that is

$$F(\mathbf{x}) = \tau(\mathbf{x}), \tag{13.2.1}$$

Stellenbosch University https://scholar.sun.ac.za

subject to a mass constraint

$$M = hw \quad \text{or} \quad w = \frac{M}{h} \text{ [for a given } h\text{]}, \tag{13.2.2}$$

where M is a PM mass constant, and dimensional constraints

$$h_1 \leq h \leq h_2 \quad \text{and} \quad w_1 \leq w \leq w_2. \tag{13.2.3}$$

To determine $\tau(\mathrm{x})$ the dimensional variable h is varied by Δh and w is calculated according to Eq. (13.2.2) in the finite element analysis (FEA) as shown in Fig. 13.2.

Fig. 13.3 indicates the maximum possible torque for a fixed magnet mass with a variation in the magnet dimensions. The magnet dimensions that give peak rated torque are chosen for the design performance evaluation presented in §13.5.

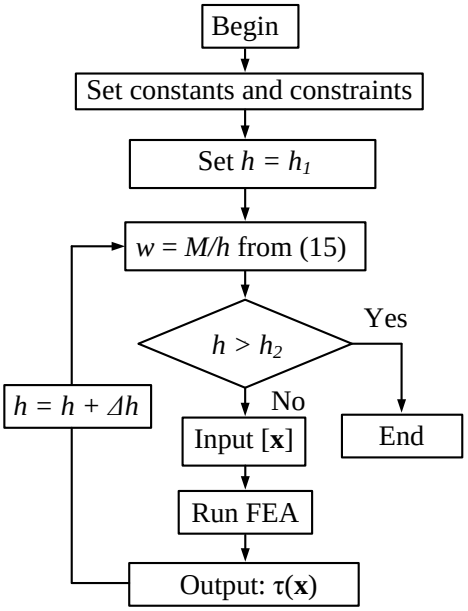

Figure 13.2: Optimization flow chart for fixed PM mass designs.

13.3 Optimization Minimizing Mass

In the second optimization the objective function $F(\mathbf{x})$ to be minimized is the mass of the coupler that is

$$F(\mathbf{x}) = u_1 M_{\mathrm{PM}}(\mathbf{x}) + u_2 M_{\mathrm{active}}(\mathbf{x}), \tag{13.3.1}$$

where u_1 and u_2 are weighting factors, M_{PM} the magnet mass and M_{active} the active mass that includes the magnet mass and core mass of the PM rotor. In

Stellenbosch University https://scholar.sun.ac.za

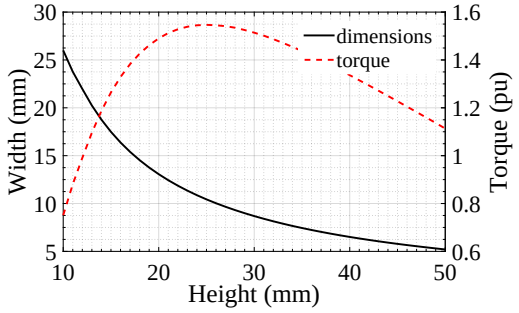

Figure 13.3: Torque results for a rotor with fixed PM mass with variation in PM width and height of the spoke-mount PM machine.

this optimization $F(\mathbf{x})$ is minimized subject to the dimensional constraints of (13.2.3) and a torque constraint of

$$\tau(\mathbf{x}) \geq \tau_{\text{rated}} = 1143.44\,\text{Nm}. \tag{13.3.2}$$

Instead of selecting the weighting factors of Eq. (13.3.1) and do the optimization, we rather determine the Pareto front curve of $M_{\text{active}}(\mathbf{x})$ versus $M_{\text{PM}}(\mathbf{x})$, and make the selection of the design from the Pareto curve. The Pareto curve is determined as explained in the flow chart of Fig. 13.4. In the flow chart the dimensional variables h and w are varied by Δh and Δw respectively.

The Pareto front results are shown in Figs. 13.5, 13.6 and 13.7. Fig. 13.5 presents the Pareto front plot for active mass versus the PM mass with the color map indicating the corresponding rated torque. The design point that yields the optimum active mass and PM mass is chosen at the knee of the Pareto plot for rated torque close to $\tau_{\text{rated}} = 1143.44$ Nm and the performance evaluation of the design is presented in §13.5. Figs. 13.6 and 13.7 indicate the variation of rated torque and PM mass with a variation in the magnet dimensions, illustrating the direct relationship between mass and energy.

13.4 General observations from the optimisations

The magnetic flux density is generally expressed as flux per unit cross-sectional area

$$\phi = BA \tag{13.4.1}$$

The design optimisations performed in this chapter are very instructive as they clearly demonstrate how the magnet dimensions influence the machine performance. It can be clearly seen that the flux concentration can be increased or decreased by varying the flux path cross-section area. The consequences thereof are highlighted by the following observations:

Stellenbosch University https://scholar.sun.ac.za

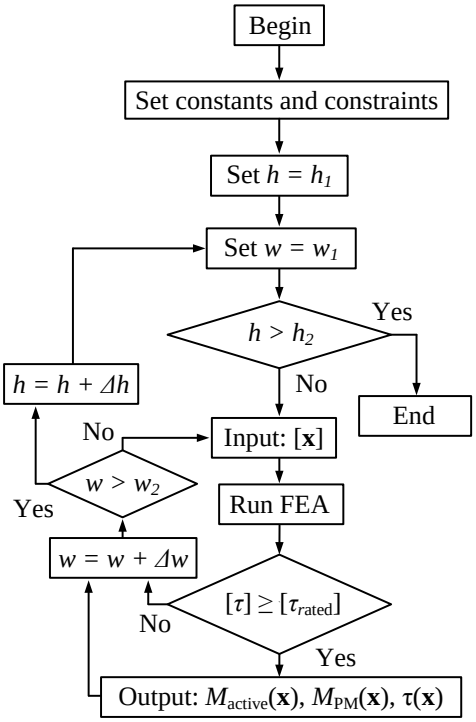

Figure 13.4: Optimization flow chart for determining a mass Pareto front with $\tau_{\text{rated}} \geq 1143.44$ Nm as constraint.

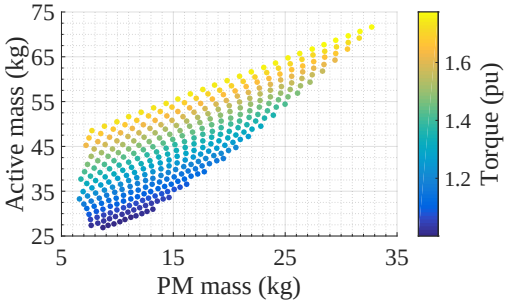

Figure 13.5: Mass Pareto front plot for $\tau_{\text{rated}} \geq 1143.44$ Nm with the color map indicating the corresponding per unit torque.

- increasing the magnet width increases the breakdown torque
- increasing the magnet height increases the rated torque

13.5 Optimised Design Performance

The two machine topologies' FE analysis performance results are presented in this section and are further supported by the FE analysis and measurement results of the reference slip-PMC shown in Fig. 13.9a in §13.6.

Stellenbosch University https://scholar.sun.ac.za

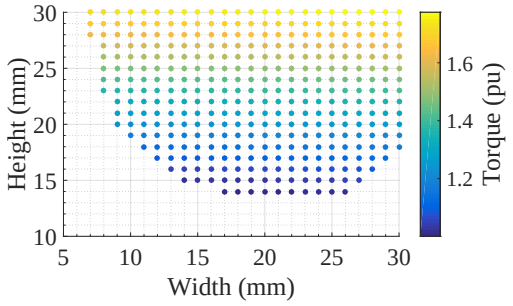

Figure 13.6: w versus h Pareto front plot for $\tau_{\text{rated}} \geq 1143.44$ Nm with the color map indicating the corresponding per unit torque.

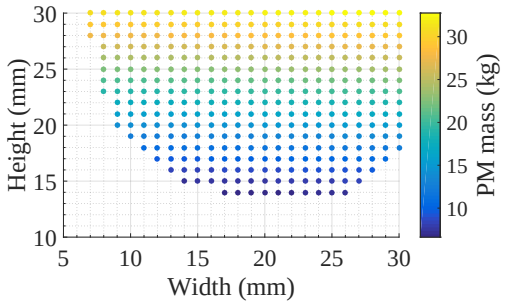

Figure 13.7: w versus h Pareto front plot for $\tau_{\text{rated}} \geq 1143.44$ Nm with the color map indicating the corresponding PM mass.

In Fig. 13.8 the torque versus slip performance curves are shown where the static and transient state simulation results of the machine designs are presented. The spoke-mount PM coupler results are for the design points selected from the design optimization results presented in §13.2 and 13.3. The torque performance results of the static spoke-mount PM coupler shown in Fig. 13.8 indicate improved performance for the same amount of magnet mass as the surface-mount PM coupler. This improved torque performance could be explained by a much higher air gap flux density due to the concentrated flux on the steel blocks produced by the spoke-mount magnets. However the active mass and rotor outer diameter of the spoke-mount PM coupler, as given in Table 13.1, is larger than that of the surface-mount PM coupler rendering it 17.9% heavier and 1.7% larger. By comparing torque per active mass as given in Table 13.1 it is found that, overall, the spoke-mount PM coupler indicates improvement in performance at rated conditions for both optimized PM rotor designs. However at breakdown torque conditions, the minimum mass PM rotor design under performs by 10.33% below the surface-mount PM coupler design. The maximum torque PM rotor design indicates a substantial improvement in performance that is 20.27% above that of the surface-mount PM coupler design.

As a case study a rated torque of 1143.44 Nm is chosen for both the surface-

Stellenbosch University https://scholar.sun.ac.za

mount and spoke-mount PM coupler. The optimum design of the spoke-mount PM coupler with a reduced PM mass and active mass gives the same rated torque. However the breakdown torque is 17.3% percent below that of the surface mount PM coupler.
The lower breakdown torque may be acceptable in wind turbine applications as wind turbines not only rely on electrical braking but also on mechanical braking. From both Fig. 13.8 and Table 13.1 it is observed that the torque-slip characteristics of the two slip-PMC topologies are different. This presents an interesting choice for designers of such machines as a variation in the torque-slip characteristic can be achieved by choosing either the spoke- or surface-mount PM coupler configuration and by varying the design dimensions.

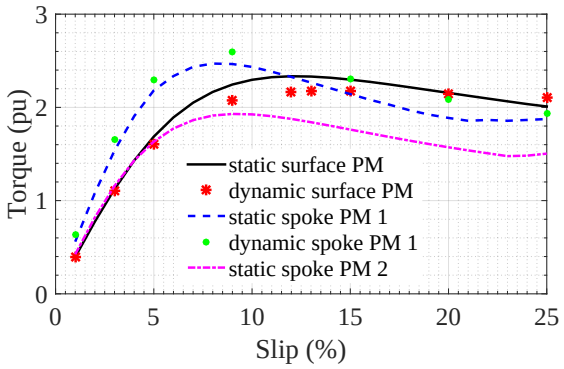

Figure 13.8: Simulation results of the spoke- and surface-mount PM machine where $\tau_{\text{rated}} = 1000$ Nm.

Table 13.1: Comparison Parameters of proposed slip-PMC topologies.

Compared Parameters	**surface mount**	**spoke 1**	**spoke 2**
PM mass (kg)	9.52	9.56	7.69
Active mass (kg)	28.41	33.5	19.59
Generated torque (Nm)	1143.44	1548.22	1157.82
Breakdown torque (Nm)	2326.88	2460.10	1929.62
$\tau/\text{m}_{\text{active}}$ (Nm/kg)	40.25	46.22	59.10
$\tau_{\text{b}}/\text{m}_{\text{active}}$ (Nm/kg)	81.90	73.44	98.50
Rated slip (%)	3	3	3
Breakdown slip (%)	15	8	9
Outer radius (mm)	316	321.3	311.3
Stack length (mm)	90	90	90
Ref speed (rpm)	150	150	150

Stellenbosch University https://scholar.sun.ac.za

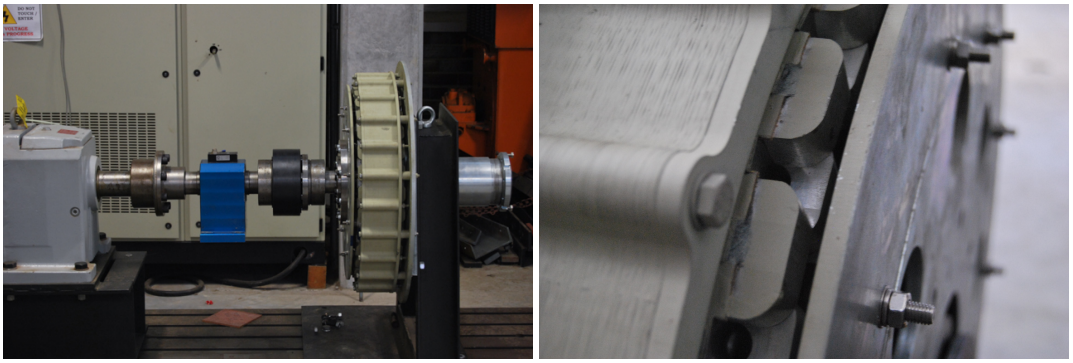

(a) (b)

Figure 13.9: (a) Surface-mount slip-PMC prototype and (b) Solid CNC cut short-circuited aluminum coils.

13.6 Slip-PMC Machine Prototype

The machine shown in Fig. 13.9a is the slip-PMC machine prototype with surface-mount PM and top-bottom coil layout. In field operating conditions, the stator of the slip-PMC is rotating at synchronous speed while the rotor is coupled to the wind turbine rotor that would be rotating at super-synchronous speed. However in the laboratory test the stator is mechanically bolted to the bench while the rotor is driven by an induction motor via a down speed gearbox drive. The induction motor is powered using flux vector control to achieve maximum possible low speed torque to drive the slip-PMC for a static test. Fig. 13.9b shows the short-circuited rotor coil of the reference slip-PMC machine with surface mount PM with a top-bottom coil layout. The prototype will in future be retrofitted with a side-by-side coil layout as shown in Fig. 8.2 and 8.1 for both the surface- and the spoke-mount slip-PMCs. A new PM rotor will in future be constructed for the spoke-mount PM machine.

The reference slip-PMC is tested under static conditions, i.e. with the PM rotor locked and thus acting as the stator of the machine. In fact the FE analysis assumes this static condition. The measurements and FE results are performed at 25°C. The test bench drive limited the test range up to a maximum torque of approximately 1000 Nm. The measurements and FE results given in Fig. 13.10 indicate good agreement. This validates the slip-PMC concept and its fundamental working principle and theory.

13.7 Summary

The sensitivity to magnet dimension variation is presented in this chapter. A torque maximisation optimisation of the spoke-mount PM machine for the fixed PM mass, which is the same as that of the surface-mount PM machine,

Stellenbosch University https://scholar.sun.ac.za

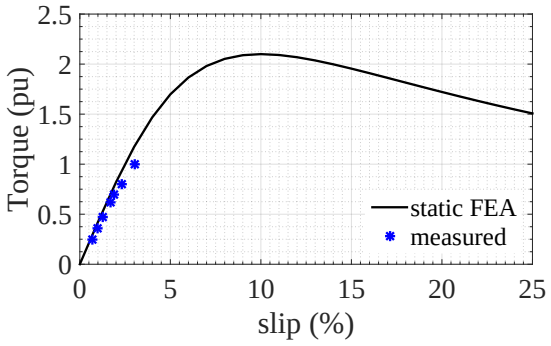

Figure 13.10: Simulation and measurement results of the reference slip-PMC operating at 25°C for $\tau_{\text{rated}} = 1000$ Nm.

performed. The PM mass minimisation is performed where for some minimum mass the machine is still able to perform to rated condition requirement. The overall performance prediction of the dynamic and static FEM model shows good agreement in terms of behaviour with the observed numerical differences. These can be attributed to the assumptions highlighted in the previous chapters. The slip-PMC prototype validates the theoretical model.

Stellenbosch University https://scholar.sun.ac.za

Part IV

Conclusions and Recommendations

Stellenbosch University https://scholar.sun.ac.za

Chapter 14

Conclusion

In this chapter an overview of conclusions from the study are given.

- In Chapter 3 the wind site is found to be very turbulent with turbulence intensity of 0.68% and has low annual mean wind speed average of 4 m/s.
- The cost model of Chapter 4 aids the decision making process as to what size turbine configuration is cost effective. It is found in the drive train cost evaluation of the NREL Phase VI and the Aero Energy wind turbine that both wind turbine configurations yield similar costs with small differences of 0.044 pu with the NREL Phase VI on the higher side of cost.
- The blade element momentum wind turbine model in Chapter 5 accurately predicts the wind turbine aerodynamic performance more rapidly. The empirical correction models implemented in the BEM model codes assist in achieving more realistic results especially under stall conditions where the flow problem considered complex.
- The computational fluid dynamics (CFD) model in Chapter 6 is numerically intensive due to the discretisation process of the Navier-Stokes equations which are non-linear equations.
- The wind turbine performance prediction in Chapter 7 is in agreement for the power curve. Discrepancies observed on the thrust curve prediction are attributed to the analytical model not accounting for the rotational effects. The wind turbine power coefficient (C_p) curve illustrates the efficiency of the wind turbine where a maximum $C_p = 0.47$ is achieved under optimum conditions.
- Two slip-PMC dq models are presented in Chapter 8 for the linear and non-linear analysis. The non-linear dq model assumes that the d-axis

Stellenbosch University https://scholar.sun.ac.za

flux due to the PM on the coils is significant, neglecting the q-axis flux component in order to simplify the analysis solution procedure. In the linear dq model the d- and q-axis flux linkage on the coils due to magnets are captured. Additionally in the linear dq model, the cross coupling effects are captured in the multiple layer modelling where the non-linear model completely ignores the effect. Discrepancies in the torque prediction is observed in the region where the machine is heavily loaded above breakdown torque. The core loss is ignored in the design optimisation, accounting for $\pm 0.10\%$ of the total power, and the only dominant loss considered is the conduction loss, accounting for $\pm 4.48\%$ of the total power.

- The analyses methods performance in Chapter 9 demonstrate that the linear analysis method has a fast convergence rate. Whereas the non-linear method convergence rate is more sensitive to the loading conditions where the convergence becomes slower with an increase in the current loading.

- In Chapter 10 the skin effect and slot leakage effect in the coils is demonstrated to affect the machine performance prediction. The dc resistance model is used in determining the internal resistance of the coils, when the fields depth of penetration in the coils is less than the coil physical depth the ac resistance model is implemented. The ac resistance model improves the torque prediction in the machine, which may be beneficial for cases where the operating frequencies are high. The slot leakage modelling technique effectively captures the saturation effects where single layer modelling gives inaccurate results.

- In Chapter 11 the end effects on the PM magnets are considered to affect the produced effective flux in the machine. The spoke-mount PM machine produces more effective flux than the surface-mount PM machine, and this is attributed to the inter pole flux leakage that occurs between adjacent magnet poles.

- In Chapter 12 it is shown that the static model assumes linearity when calculating the induced armature voltage and currents. The spatial flux variations are not considered in the analytical model which is suspected to result in a lower induced eddy current prediction. In the static FEM model the induced currents are predicted as source currents, whereas in the dynamic model the induced currents emerge from the model governing equations. A frequency sweep shows the peak current obtained from the static and dynamic model to be in agreement. Observing the induced current waveforms and the harmonics, one finds 3rd and 5th time harmonic components which are not present in the static case, which are

Stellenbosch University https://scholar.sun.ac.za

suspected to be responsible for the discrepancies in the torque performance prediction.

- Maximum torque is obtained for the spoke-mount PM configuration with some magnet pitch for the same amount of PM materials as that of the surface-mount PM configuration. The spoke-mount PM machine has shown higher torque performance indicating that that it has a potential of outperforming the surface-mount PM machine configuration.
- The slip-PMC prototype under test rig conditions agrees well with the static analysis FEM methods.

Stellenbosch University https://scholar.sun.ac.za

Chapter 15

Recommendations

The recommendations provided in this chapter are reached from the outcomes and challenges of the research scope components.

- The analysis methods presented in this thesis are good estimators of the machine performance, however require further scrutiny as to how they can model the harmonic components of the currents, as this could lead too improved performance prediction as those high frequency components can also add to the effective resistance of the coils.
- The CFD wind turbine performance results need futher verification by means of a transient analysis since the moving mesh methods is considered more accurate than the static mesh method.
- The cost modelling of small-scale wind turbines in case of scrutinize for areas where cost can be minimised is imperative in order to allow transparency for adopters of such technologies to understand their costs.
- Fields measurements of the wind turbine needs to be conducted to establish the true performance of the wind turbine blades and where possible calibrate the wind turbine models.
- other analytical techniques of modelling induction machines can be employed, such as in literature [55–57] whereby Poison's, Laplace and Helmholtz equations are resolved in the machine.
- The energy stored in PM and its effectiveness in electrical machines can be studied by means of the spok-mount PM machine. This machine configuration in FEM has shown to be sensitive to the Neumann (zero-potential field boundary). Placing this boundary closer to spoke-mount PM such that no flux leakage is considered, the performance prediction appears to increase in torque and induced current. In literature [58, 59] the stored energy in permanent magnets evaluated where a procedure of determining the energy in a permanent magnet is discussed. Given that

Stellenbosch University https://scholar.sun.ac.za

more energy is available in the magnet than what the electrical machine produces, raises questions as to how much of this energy is actually not utilised and how can one quantify the losses that occur in the energy transfer from the magnet to the generated effective magnetic field that is responsible for the generated torque.

Stellenbosch University https://scholar.sun.ac.za

Appendices

Stellenbosch University https://scholar.sun.ac.za

Appendix A

Spalart-Allmaras Turbulence Model

The Spalart-Allmaras turbulence model is a one equation model based on a modified turbulence viscosity, $\tilde{\nu}$. The model is expressed as follows:

$$\frac{D}{Dt}(\rho\tilde{\nu}) = \nabla\cdot(\rho D_{\tilde{\nu}}\tilde{\nu}) + \frac{C_{b2}}{\sigma_{\nu_t}}\rho|\nabla\tilde{\nu}|^2 + C_{b1}\rho\tilde{S}\tilde{\nu}(1-f_{t2}) - \left(C_{w1}f_w - \frac{C_{b1}}{\kappa^2}f_{t2}\right)\rho\frac{\tilde{\nu}}{\tilde{d}^2} + S_{\tilde{\nu}} \tag{A.0.1}$$

the f_{t2} term is not implemented not implemented in OpenFOAM. The turbulence viscosity is obtained using

$$\nu_t = \tilde{\nu} f_{v1} \tag{A.0.2}$$

where the function f_{v1} is given by

$$f_{v1} = \frac{\chi^3}{\chi^3 + C_{v1}^3} \tag{A.0.3}$$

and

$$\chi = \frac{\tilde{\nu}}{\nu} \tag{A.0.4}$$

The default model coefficients are as given in Table A.1.

Table A.1: Default Turbulence model coefficients

σ_{ν_t}	C_{b1}	C_{b2}	C_{w1}	C_{w2}	C_{w3}	C_{v1}	C_s
$2/3$	0.1355	0.622	$\frac{C_{b1}}{\kappa^2} + \frac{1+C_{b2}}{\sigma_{\nu_t}}$	0.3	2	7.1	0.3

Stellenbosch University https://scholar.sun.ac.za

List of References

[1] V. K. M. Cheng and G. P. Hammond, "Life-cycle energy densities and land-take requirements of various power generators: A uk perspective," *Elsvier, Journal of the Energy Institute*, vol. 90, pp. 201–213, 2017.

[2] WindPower, "Small-scale wind energy: Policy insights and practical guidance," in *The Physics of Granular Media*, H. Hinrichsen and D. Wolf, Eds. Weinheim: Wiley-VCH, 2004, pp. 299–324.

[3] N. Dumakude, "Validation of bem using cfd mrf coupled with axial and radial induction factors," AIAA. Denver, CO: Aviation Forum, Jun 2017, 8th AIAA Theoretical Fluid Mechanics Conference.

[4] N. Dumakude and M. J. Kamper, "Performance evaluation of slip couplers with spoke- and surface-mount pm for wind energy applications," *IEEE, ECCE*, Oct 2017.

[5] IEC 61400.2-2006, "Wind turbines part 2. design requirements for small wind turbines," International Electro-technical Commission, Tech. Rep., March 2006.

[6] W. E. Foundation, "History of wind energy." [Online]. Available: http://www.windenergyfoundation.org

[7] R. von Mises, *Theory of Flight*, 1st ed. Dover Publications, Jun 1959.

[8] H. Glauert, *Airplane Propellers: in W.F. Durand (ed) Aerodynamic Theory.* Berlin: Division L, Julius Springer, vol. 4.

[9] U. S. Paulsen, "Konceptundersogelse nordtank ntk 500/41. strukturelle laster (in danish)," *Risø-I-936(DA)*, Nov 1995.

[10] M. O. L. Hansen, *Aerodynamics of Wind Turbines*, second edition ed. Earthscan UK and USA.

[11] C. Bak, P. Fuglaang, N. N. Sorensen, H. Aagaard Madsen, W. Z. Shen, and J. N. Sorensen, "Airfoil characteristics for wind turbines," *Risø-R*, no. No. 1065(EN), 1999.

Stellenbosch University https://scholar.sun.ac.za

[12] H. K. Versteeg and W. Malalasekera, *An Introduction to Computational Fluid Dynamics: The Finite Volume Method*, 2nd ed. Pearson and Prentice-Hall, 2007.

[13] F. R. Menter, "Two-equation eddy-viscosity turbulence model for engineering applications," *AIAA Journal*, vol. 32, Aug 1994.

[14] B. E. Launder and D. B. Spalding, "The numerical computation of turbulent flows," *Computer Methods in Applied Mechanics and Engineering 3*.

[15] D. C. Wilcox, "Formulation of the $k-\omega$ turbulence model revisited," *45th AIAA Aerospace Sciences Meeting and Exhibit*, January 2007.

[16] M. Cheah-Mane, J. Liang, and N. Jenkins, "Permanent magnet synchronous generator for wind turbines: Modelling, control and inertial frequency response," *IEEE Power Engineering Conference (UPEC)*, Sept 2014, 49th International Universities.

[17] H. Li and Z. Chen, "Overview of different wind generator systems and their comparisons," *IET Renewable Power Generation*, vol. 2, no. 2, pp. 123–138, 2008.

[18] Z. Mouton, "Modelling and design of an eddy current coupling forf slip-synchrnous permanent magnet wind generators," Master's thesis, Department of Electrical and Electronic Engineering, Stellenbosch University, March 2013.

[19] J. H. J. Potgieter, "Optimal topology and critical evaluation of slip synchronous permanent magnet wind generator," Ph.D. dissertation, Department of Electrical and Electronic Engineering, Stellenbosch University, Apr 2014.

[20] D. K. Ockhuis, A. S. Erasmus, and M. J. Kamper, "Small-scale geared turbine system with slip-synchronous technology," *WindAc Africa*, 2016.

[21] J. H. J. Potgieter and M. J. Kamper, "Optimum design and technology evaluation of slip permanent manget generators for wind energy applications," *IEEE ECCE*, pp. 2349–2349, Sept 2012.

[22] ——, "Design of new concept permanent magnet induction wind generator," *IEEE Energy Conversion Congress & Expo (ECCE)*.

[23] J. J. J. Van Wyk and M. J. Kamper, "Simplified analysis technique for double layer non-overlap multiphase slip permanent magnet couplings in wind energy applications," *IEEE IEMDC*, pp. 1217–1223, 2011.

Stellenbosch University https://scholar.sun.ac.za

[24] F. Zhao, T. A. Lipo, and B. Kwon, "A novel dual-stator axial-flux spoke-type permanent magnet vernier machine for direct-drive applications," *IEEE, Transactions on Magnetics*, vol. 5, Nov 2014.

[25] A. Genc, M. Erisoglu, A. Pekgor, G. Oturanc, A. Hepbasli, and K. Ulgen, "Estimation of wind power potential using weibull distribution," *Energy Sources*, vol. 27, no. 9, pp. 809–822, Aug 2006.

[26] A. J. Cavalo, "High capacity factor wind systems," Center for Energy and Environmental Studies, Princeton University, Princeton, NJ, 08544, Tech. Rep., May 1995.

[27] C. G. Justus, W. R. Hargraves, A. Mikhail, and D. Grabber, "Methods for estimating wind speed frequency distributions," *Appl Meteorol*, vol. 17, no. 350, p. 3, 1978.

[28] T. Burton, N. Sharpe, and E. Bossanyi, *Wind Energy Handbook*. John Wiley & Sons, 2001.

[29] J. Wieringa, "Gust factors over open water and built-up country," *Boundary-Layer Meteorology 3*, pp. 424–441, 1973.

[30] J. Tangler, B. Smith, and D. Jager, "Seri advanced wind turbine blades," National Renewable Energy Laboratory, Golden, CO, Tech. Rep., Feb 1992.

[31] G. Weinzierl, "A bem based simulation-tool for wind turbine blades with active flow control elements," Institut Für Stromömungsmechanik Und Technische Akustik Fachgebiet Für Experimentelle Strömungsmechanik, Apr 2011.

[32] D. Marten and J. Wendler, *QBlade Guideline v.06*, Technical University of Berlin, Jan 2013. [Online]. Available: http://www.q-blade.org

[33] M. D. Lennie, "Development of the qfem solver: The development of modal analysis code for wind turbine blades in qblade," Master's thesis, KTH School of Industrial Engineering and Management, Energy Technology, Division of Heat and Power, Royal Instutue of Technology, Stockholm, Oct 2013.

[34] J. J. J. Van Wyk, "Design and evaluation of medium speed geared direct grid-connected wind generator drive train with specific focus on slip permanent magnet coupling," Master's thesis, Department of Electrical and Electronic Engineering, Stellenbosch University, Stellenbosch, South Africa, Dec 2015.

Stellenbosch University https://scholar.sun.ac.za

[35] M. Drela, "Xfoil: An analysis and design system for low reynolds number airfoils," MIT Dept. of Aeronautics and Astronautics, Cambridge, Masachusetts, Tech. Rep., 1989. [Online]. Available: https://web.mit.edu/drela/Public/papers/xfoil_sv.pdf

[36] B. Montgomerie, "Methods for root effects, tip effects and extending the angle of attack range to ±180° with application to aerodynamics for blades on wind turbines and propellers: Scientific report," Swedish Defence Research Agency, Sweden, Tech. Rep., 2004.

[37] S. J. Miley, "A catalogue of low reynolds number airfoils data for wind turbine applications," NREL, Tech. Rep.

[38] P. Giguère and M. S. Selig, "New airfoils for small horizontal axis wind turbines," *Journal of Solar Energy*, May 1998.

[39] M. M. Yelmule and E. Anjuri, "Cfd predictions of nrel phase vi rotor experiments in nasa/ames wind tunnel," *International Journal of Renewable Energy Research*, vol. 3, no. 2, 2013.

[40] H. Rahimi, B. Dose, B. Stoevesandt, and J. Peinke, "Investigation of the validity of bem for the simulation of wind turbines in complex load cases and a comparison with experiments and cfd," 2014. [Online]. Available: https://www.windeurope.org/summit2016/conference/submit-an-abstract/pdf/348878262528.pdf

[41] F. R. Menter, M. Kuntz, and R. Langry, "Ten year of industrial experience with the sst turbulence model." Begell House, Redding, CT: Proceeding of the Fourth International Symposium on Turbulence, Heat and Mass Transfer, 2003.

[42] P. R. Spalart and S. R. Allmaras, "A one-equation turbulence model for aerodynamic flow," *La Rocherche Aérospatiale*, vol. 1, pp. 5–21, 1994.

[43] RISO, *Guideline for Design of Wind Turbines*, second edition ed. Denmark: Det Norske Veritas, Copenhagen and Wind Energy Department, Risø, 2002.

[44] J. H. J. Potgieter and M. J. Kamper, "Design of new concept permanent magnet induction wind generator," *IEEE Energy Conversion Congress and Exposition*, pp. 2403–2408, 2010.

[45] F. Libert and J. Soulard, "Investigation of pole-slot combinations for permanent-magnet machines with concentrated windings," *Proceedings of the International Conference on Electrical Machines (ICEM)*, 2004.

Stellenbosch University https://scholar.sun.ac.za

[46] B. Aslan, E. Semail, J. Korecki, and L. J., "Slot/pole combinations choice for concentrated multiphase machines dedicated to mild-hybrid applications," *IECON'11, IEEE International Conference On Industrial Applications of Electronics*, pp. 3698–3703, Nov 2011.

[47] P. Svetlik and K. Hruska, "Construction of the fspm machine and its measurement in comparison with modeled results," *IEEE, ECCE*, Sept 2016.

[48] E. E. Montavlo-Ortiz, S. N. Foster, J. G. Cintron-Rivera, and E. G. Strangas, "Comparison between a spoke-type pmsm and a pmasynrm using ferrite magnets," *IEEE, IEMDC*, May 2013.

[49] N. Mohan, T. M. Undeland, and W. P. Robbins, *Power Electronics: Converters, Applications, and Design*, 3rd ed. Wiley, Nov 2002.

[50] A. E. Fitzgerald, C. Kingsley, and S. D. Umans, *Electric Machinery*, 6th ed. McGraw-Hill, 2002.

[51] N. Raabe, "A 2d approximation of standard electrical steel losses and permeability," *Springer Verlag*, pp. 367–371, Jul 2014.

[52] B. Guru and H. Hiziroˇ glu, *Electromagnetic Field Theory Fundamentals*, 2nd ed. Cambridge University Press.

[53] V. B. Honsinger, "Theory of end-winding leakage reactance," *AIEE. Power Apparatus and Systems*, vol. 78, no. 3, Aug 1959.

[54] S. E. Skaar, O. Krovel, and R. Nilssen, "Distribution, coil-span and winding factors for pm machines with concentrated windings," *IEEE ICEM*, 2006.

[55] T. Lubin, S. Mezani, and A. Rezzoug, "Analytic calculation of eddy currents in the slots of electrical machines: Application to cage rotor induction motors," *IEEE Transactions on Magnetics*, vol. 47, Nov 2011.

[56] K. Boughrara, N. Takorabet, R. Ibtiouen, O. Touhami, and F. Dubas, "Analytical analysis of cage rotor induction motors in healthy, defective and broken bars conditions," *IEEE Transaction on Magnetics*, Jan 2014.

[57] S. R. Holm, H. Polinder, and J. A. Ferreira, "Analytical modelling of a permanent-magnet synchronous machine in a flywheel," *IEEE Transactions on Magnetics*, vol. 43, no. 5, May 2007.

[58] P. Campbell, "Comments on energy stored in permanent magnets," *IEEE Transactions on Magnetics*, vol. 36, no. 1, Jan 2000.

[59] H. C. Lovatt and P. A. Watterson, "Energy stored in permanent magnets," *IEEE Transactions on Magnetics*, Jan 1999.